



Carbon Cycle Instability for High-CO₂ Exoplanets: Implications for Habitability

R. J. Graham¹ and R. T. Pierrehumbert² ¹ Department of Geophysical Sciences, University of Chicago, 5734 S Ellis Ave. Chicago, IL 60637, USA; arejaygraham@uchicago.edu² Department of Atmospheric, Oceanic, and Planetary Physics, University of Oxford, Clarendon Laboratory, Parks Rd. Oxford, OX1 3PU, UK

Received 2023 July 27; revised 2024 April 24; accepted 2024 April 26; published 2024 July 12

Abstract

Implicit in the definition of the classical circumstellar habitable zone (HZ) is the hypothesis that the carbonate-silicate cycle can maintain clement climates on exoplanets with land and surface water across a range of instellations by adjusting atmospheric CO₂ partial pressure ($p\text{CO}_2$). This hypothesis is made by analogy to the Earth system, but it is an open question whether silicate weathering can stabilize climate on planets in the outer reaches of the HZ, where instellations are lower than those received by even the Archean Earth and CO₂ is thought likely to dominate atmospheres. Since weathering products are carried from land to ocean by the action of water, silicate weathering is intimately coupled to the hydrologic cycle, which intensifies with hotter temperatures under Earth-like conditions. Here, we use global climate model simulations to demonstrate that the hydrologic cycle responds counterintuitively to changes in climate on planets with CO₂-H₂O atmospheres at low instellations and high $p\text{CO}_2$, with global evaporation and precipitation decreasing as $p\text{CO}_2$ and temperatures increase at a given instellation. Within the Maher & Chamberlain (or MAC) weathering formulation, weathering then decreases with increasing $p\text{CO}_2$ for a range of instellations and $p\text{CO}_2$ typical of the outer reaches of the HZ, resulting in an unstable carbon cycle that may lead to either runaway CO₂ accumulation or depletion of CO₂ to colder (possibly snowball) conditions. While the behavior of the system has not been completely mapped out, the results suggest that silicate weathering could fail to maintain habitable conditions in the outer reaches of the nominal HZ.

Unified Astronomy Thesaurus concepts: [Habitable planets \(695\)](#); [Exoplanets \(498\)](#); [Exoplanet atmospheres \(487\)](#)

1. Introduction

As conventionally defined (Kasting et al. 1993; Kopparapu et al. 2013), the habitable zone (HZ) is predicated on habitable conditions being maintained by the joint greenhouse effect of CO₂ and water vapor, possibly as modified by background gases such as N₂. The inner edge is defined by the runaway greenhouse threshold, in which water vapor provides the dominant greenhouse effect. The outer edge is defined by the maximum CO₂ greenhouse effect, in which the dominant greenhouse effect is provided by CO₂. Actual habitability within the HZ is contingent on the planet having an atmosphere, and moreover having CO₂ in the right range to permit surface liquid water.

The conventionally defined HZ only takes into account thermodynamic and radiative constraints on surface temperature, though it is generally an implicit assumption that silicate weathering feedbacks adjust atmospheric CO₂ to a range supporting surface liquid water, supposing thermodynamic and radiative constraints permit such a range to exist. The implicit assumption, needed to assure actual habitability, is that geochemical feedbacks keep CO₂ from getting too high in concentration near the inner edge and keep CO₂ from staying too low near the outer edge; without such a thermostat mechanism, habitability would be contingent on fortuitous fine-tuning of CO₂ concentration. However, there is growing recognition that the geochemistry of the deep carbon cycle also provides constraints on CO₂, and might fail to keep CO₂ in the required range (Noack et al. 2017; Foley & Smye 2018; Foley 2019). On this basis one can define a *geochemical HZ*, which

layers constraints from the deep carbon cycle on the usual thermodynamic and radiative constraints. In addition to a carbon cycle equilibrium existing in a habitable range of CO₂, it is required that the equilibrium be a stable equilibrium. Stability requires that weathering rates increase with increasing CO₂. In this article, through coupled climate-weathering modeling, we exhibit some indications that the geochemical HZ may be significantly contracted relative to the conventional HZ, via destabilization of the carbon cycle equilibrium in the outer reaches of the conventional HZ.

The estimated width of the HZ is an important input in the design of the next generation of space telescopes, some of which hope to observe and characterize the atmospheres of a handful of “Earth analogs” (Guimond & Cowan 2018; The LUVUOIR Team 2019; Gaudi et al. 2020; Quanz et al. 2021). In particular, a narrower HZ requires a larger telescope to find a given number of these planets (e.g., Kasting & Harman 2013), so, in addition to potentially determining the fate of untold numbers of extraterrestrial worlds, the additional constraints defining the geochemical HZ may have practical implications for space mission design.

Intensification of the hydrologic cycle with surface temperature is one of the most robust features to emerge from studies modeling Earth’s warmer future climate under the influence of higher CO₂ (Held & Soden 2006; O’Gorman & Schneider 2008; Kundzewicz 2008; O’Gorman et al. 2012; Allan et al. 2020), and the same basic behavior emerges under diverse simulated exoplanetary climate conditions (Xiong et al. 2022). Earth’s global-mean precipitation rate is consistently predicted to increase approximately linearly with global-mean surface temperature at $\approx 2\% \text{ K}^{-1}$ (e.g., Held & Soden 2006; O’Gorman & Schneider 2008; O’Gorman et al. 2012), lagging well behind the 7% that would be expected from a naive application of the Clausius–Clapeyron relation because of

simultaneous slowdown in atmospheric circulation under warming conditions (Vecchi et al. 2006). This coupling between hydrologic cycling and surface temperature is a fundamental component of some formulations of the silicate weathering feedback model (Walker et al. 1981, hereafter “the WHAK weathering model”), particularly the model described in Maher & Chamberlain (2014, hereafter “the MAC weathering model” or “MAC formulation”), where it becomes the primary mechanism by which silicate weathering is sensitive to global surface temperature, suggesting precipitation’s temperature sensitivity may play a crucial role in the long-term regulation of the climates of Earth and exoplanets with carbonate-silicate cycles like Earth’s (Graham & Pierrehumbert 2020).

Given the potential importance of precipitation–climate coupling for climate stability and long-term planetary habitability, it is an underappreciated fact that the energetic cost of evaporating water into the atmosphere places a serious constraint on the maximum rate of global-mean precipitation a planet at a given instellation can sustain (Pierrehumbert 1999, 2002; O’Gorman & Schneider 2008; Le Hir et al. 2009; Pierrehumbert 2010; O’Gorman et al. 2012). This is readily apparent from a bulk representation of the steady-state surface energy budget:

$$S_{\text{abs}} = H_{\text{rad,sens}} + L, \quad (1)$$

where S_{abs} is the absorbed instellation at the surface, $H_{\text{rad,sens}}$ is the combined flux from long wave (infrared) and sensible (dry turbulent) heating/cooling of the surface, and L is the latent heat flux from the surface. If we raise the concentration of CO_2 enough for a large amount of water vapor to accumulate in the boundary layer, long-wave cooling of the surface will be suppressed and boundary layer stability will increase as the temperature contrast between the ground and the overlying air is reduced (Pierrehumbert 2002, 2010; O’Gorman & Schneider 2008). Each of those effects acts to reduce the magnitude of the term $H_{\text{rad,sens}}$, while the evaporative flux (and therefore L) increases, which at steady state is equivalent to the statement that the mean precipitation increases (Pierrehumbert 1999). Eventually, at high enough temperatures, the latent heat flux dominates the right side of the equation and approaches the value of the absorbed instellation, such that nearly all incoming radiation goes into driving evaporation. Beyond this point, the only way to drive evaporation higher is to form an inversion layer at the surface, such that a sensible heat flux can be directed downward into the surface (i.e., turning $H_{\text{rad,sens}}$ negative so that L can exceed S_{abs} ; Pierrehumbert 2002; O’Gorman et al. 2012), but the magnitude of this possible overshoot is limited (O’Gorman & Schneider 2008; Pierrehumbert 2010). Thus the instellation absorbed at the surface of a planet places a fairly robust upper cap on global rates of precipitation. Global climate model (GCM) simulations have suggested that this phenomenon may have throttled weathering rates during the hot, high- CO_2 aftermath of Earth’s snowball events (Le Hir et al. 2009) and low-dimensional exoplanet weathering and climate models have recently included a crude parameterization of the effect (Graham & Pierrehumbert 2020; Coy 2022), but the implications of a maximum global precipitation rate for the stability of exoplanetary climate are still largely unexplored.

Here, for the first time, we combine GCM simulations with the continental weathering model introduced in MAC and elaborated in Winnick & Maher (2018), Graham & Pierrehumbert (2020), Hakim et al. (2021) to investigate carbon cycle stability in the outer reaches of the HZ. Treatment of seafloor weathering in analogous conditions is left to future work. The MAC weathering model accounts for the fact that formation of secondary minerals (i.e., clays and silica) in the weathering zone can lead to chemical equilibration that caps the concentration of weathering products in runoff, shifting the main temperature feedback in the carbonate-silicate cycle from the kinetics of silicate dissolution (e.g., WHAK) to the temperature sensitivity of hydrologic cycling. The combination of reduced top-of-atmosphere (TOA) instellation and elevated albedo from high CO_2 partial pressures ($p\text{CO}_2$) places strong upper bounds on the amount of global precipitation planets in low-instellation regimes can generate. This led us to suggest based on global-mean simulations in Graham & Pierrehumbert (2020) that the energetic limit on precipitation might lead to warmer climates than previously expected in the outer reaches of the HZ. Full three-dimensional GCMs conform to the energy limit on precipitation, but also capture aspects of the hydrological cycle inaccessible to energy-balance modeling. We find that when weathering is calculated according to the MAC formulation using GCM-based precipitation and temperature fields, the carbonate-silicate cycle transitions from a negative, stabilizing feedback for planets at high instellation and low $p\text{CO}_2$ to a positive, destabilizing feedback for planets with energetically limited hydrology due to low instellation and high $p\text{CO}_2$.

The resulting climate-carbon equilibrium in the latter regime, in which volcanic outgassing is balanced by sinks due to silicate weathering, is unstable. If the equilibrium is displaced on the low- CO_2 side, the CO_2 will continue to decrease until it finds a new equilibrium with low CO_2 , resulting in a colder, potentially snowball, state. If displaced toward the high- CO_2 side, CO_2 will continue to accumulate in the atmosphere, resulting in either an uninhabitably hot state or a state with a temperate liquid CO_2 ocean, depending on instellation. In contrast, when weathering is calculated according to Walker et al. 1981 (which exhibits a greater degree of direct temperature dependence), the carbon cycle uniformly displays negative-feedback behavior in the high- CO_2 outer portion of the HZ we have probed as well as in the inner low- CO_2 portion.

In essence, our calculations have identified a forbidden zone of the climate/carbon equilibrium extending to at least the range of CO_2 between approximately 1 and 4 bars, and instellation between 675 and 1000 W m^{-2} , within which the climate/carbon equilibrium is unstable. However, because of limitations in our modeling framework, we have not identified the precise boundaries of the forbidden zone, and in particular have not been able to probe instellations all the way to the outer edge of the conventional HZ. The instability in the forbidden zone implies a novel form of hysteresis in the climate-carbon system. Climates in the forbidden zone will be attracted to low or high CO_2 outside the forbidden zone, but we are not currently able to precisely identify these attractors, though we offer some speculations about what they might be. While our results are not definitive, they have uncovered some very novel behavior in the outer reaches of the conventional HZ, which may restrict the geochemical HZ to a smaller range of orbital distances than the conventional HZ.

Table 1

Table with Checkmarks Indicating the Combinations of Substellar TOA Instellation (S ; Columns) and CO_2 Partial Pressure ($p\text{CO}_2$; Rows) Used in the Simulations Presented in This Study

	S (W m^{-2})				
	675	750	800	1000	1250
$p\text{CO}_2$ (bars)
2×10^{-4}	✓
3×10^{-4}	✓
4×10^{-4}	✓
1	...	✓	✓	✓	...
2	✓	✓	✓	✓	...
3	✓	✓	✓
4	✓

Note. The simulations with $p\text{CO}_2 < 1$ bar (marked bold) are supplemented by 1 bar of N_2 , while those with $p\text{CO}_2 > 1$ bar have no atmospheric N_2 .

In Section 2, we describe the models and methods we applied. In Section 3, we describe the results of our simulations. In Section 4, we discuss the implications of these results. In Section 5, we discuss some important caveats concerning our results, and in Section 6 we summarize our main findings.

2. Methods

2.1. Climate Model

To simulate planetary climate, we use the open-source Isca GCM framework (Vallis et al. 2018), which solves the hydrostatic pressure-coordinate primitive equations on a sphere using a pseudo-spectral dynamical core. The model has been used in a wide variety of planetary climate contexts (e.g., Penn & Vallis 2018; Thomson & Vallis 2019a, 2019b; Yang et al. 2019b). We present 14 GCM simulations, with 11 in high- $p\text{CO}_2$, low-instellation model configurations and three with more Earth-like configurations (discussed further below; see also Table 1). All simulations have a T42 horizontal resolution (64 latitudes, 128 longitudes) and 40 vertical sigma-pressure layers. We employ built-in Isca features, notably a simple Betts–Miller convective relaxation scheme (Betts & Miller 1993) and a bucket hydrology configuration governing evaporation (Vallis et al. 2018), modeled after the treatment of soil in Manabe (1969). Boundary layer fluxes are treated with Isca’s default Monin–Obukov scheme (Vallis et al. 2018) as in Frierson et al. (2006). The land configuration in the simulations we present consists of a simplified, topography-free polygonal representation of modern-day continents (Figure 1), but qualitatively similar results emerged from a smaller set of simulations with a single large, equatorial continent (not shown), suggesting the basic physical phenomena in play are insensitive to continental configuration. A full description of the Isca model can be found in Vallis et al. (2018), and the model outputs and postprocessing scripts used for this article are available for download (Graham & Pierrehumbert 2024). Planetary surfaces are given a uniform albedo of 0.05, comparable to that of Earth’s seawater at the insolation-weighted global-mean zenith angle of $\approx 48.19^\circ$ (Li et al. 2006; Cronin 2014). This is a conservative choice, since applying a higher albedo to land would reduce the amount of sunlight absorbed at the planetary surface and lower the energetic limit

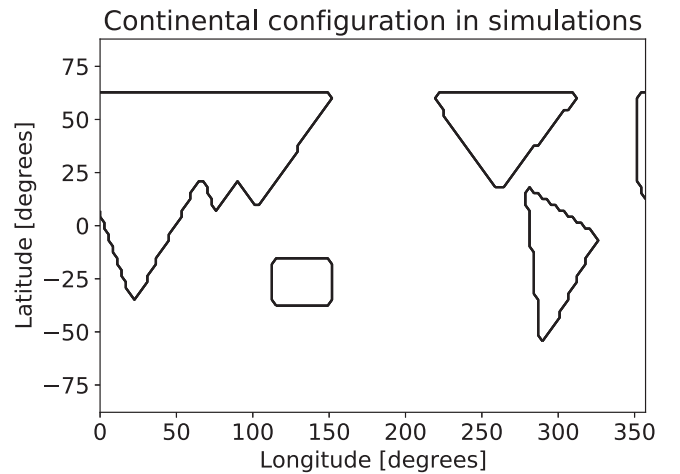


Figure 1. The continental configuration used in the presented simulations.

on precipitation. We use Isca’s slab ocean configuration with a reduced, 10 m mixed-layer depth to accelerate convergence of the simulations to energetic steady state. We discuss the potential limitations of a slab ocean configuration in Section 5.5. Obliquity and eccentricity are set to zero, so there is no seasonal cycle. The day length in all simulations is 24 hr, so our results are specific to rapidly rotating planets like Earth. Isca’s current implementation is cloud-free, a significant simplification, but this study already explores a number of highly novel aspects at the intersection of hydrology and weathering, so it was our judgment that it is at this point best to stick to the relatively robust clear-sky physics without layering on additional uncertainties arising from the many different ways cloud feedbacks can behave. Certainly, exploration of the extent to which the behavior we reveal survives the addition of cloud effects is a prime target for future research. It is worth noting that under high- CO_2 conditions, low-lying high-albedo water clouds are predicted to decrease substantially in extent due to the inhibition of cloud-top radiative cooling in a highly opaque atmosphere (Schneider et al. 2019; Goldblatt et al. 2021), so the approximation may be less grave under those conditions; even if this effect carries over to the higher- CO_2 regime in the present study, the effect of higher-altitude water clouds could be significant. CO_2 clouds can form for planets quite close to the outer edge of the HZ, but we only present simulations where CO_2 is subsaturated throughout the atmosphere, so although CO_2 clouds may be relevant in similar climates with slightly higher $p\text{CO}_2$ or lower temperatures (e.g., Kitzmann 2017), their neglect has no impact on our results. The model also excludes land or sea ice, so the ice–albedo feedback (e.g., Sellers 1969) is not in play, but this is not a serious issue for the warm climates we are examining, all of which sport little or no surface area with temperatures below freezing (as described in Section 3.1). Further, the ice–albedo feedback is weakened significantly under thick CO_2 atmospheres, which reduce the impact of changes to the surface albedo on planetary energy budgets (Von Paris et al. 2013).

Radiative transfer calculations coupled to Isca’s dynamics are carried out with the SOCRATES code (Edwards & Slingo 1996), using the correlated- k method to solve the plane-parallel, two-stream approximated radiative transfer equation with scattering for atmospheres irradiated by a solar (G -star) spectrum. In high-instellation, low- $p\text{CO}_2$ simulations, we used

the standard, validated spectral files used by the UK Met Office in the latest iteration of its Unified Model to simulate Earth’s climate (Walters et al. 2019). For high- $p\text{CO}_2$ model configurations, we used a spectral file from NASA GISS’s ROCKE-3D (Way et al. 2017) database and created for GCM modeling of the ancient Martian atmosphere, similar (though not identical) in construction to that used in Guzewich et al. (2021; Eric T. Wolf 2022, private communication). The file is valid for atmospheres up to 10 bars with $>90\%$ CO_2 and temperatures up to 400 K, with some loss of accuracy above 310 K (though we compared TOA fluxes from this model at high temperatures with those generated using a high-resolution 318-band spectral file used in Graham et al. (2022) and found the output from the GCM stayed within 5 W m^{-2} of the higher-resolution calculations). Rayleigh scattering is interactively calculated with coefficients included in SOCRATES for the relevant gases. For CO_2 , opacity coefficients were tabulated and derived from the HITRAN database, making use of line-by-line and collision-induced absorption coefficients, along with sub-Lorentzian line broadening and self-broadening (Perrin & Hartmann 1989; Baranov et al. 2004; Gordon et al. 2017), and similarly for H_2O , which included line-by-line and collision-induced absorption coefficients and the H_2O MT-CKD continuum, along with broadening coefficients that are unfortunately calculated with respect to Earth air (Mlawer et al. 2012; Gordon et al. 2017), which may somewhat underestimate water opacities at high temperatures (Pierrehumbert 2010). We note that the CO_2 continuum spectrum is uncertain at high temperatures and pressures, which introduces a potentially significant source of error into our calculations (e.g., Halevy et al. 2009; Wordsworth et al. 2010).

With one exception, each simulation was run until the TOA and surface energy fluxes were balanced to within $<1\%$ and then for at least a year further, with stated results coming from averages over the final year of data for each simulation. The three low- $p\text{CO}_2$ simulations have N_2 -dominated atmospheres, surface pressures of 1 bar, and CO_2 concentrations of 200, 300, and 400 parts per million by volume (ppmv), all irradiated by TOA instellation of $S = 1250 \text{ W m}^{-2}$. The 11 high- $p\text{CO}_2$ simulations have TOA substellar shortwave instillations of $S = 675, 750, 800,$ or 1000 W m^{-2} , and CO_2 partial pressures of 1, 2, 3, or 4 bars (see Table 1). All simulations have atmospheric H_2O content determined by Isca’s hydrologic cycle. The simulation with 3 bars of CO_2 irradiated by $S = 800 \text{ W m}^{-2}$ is the exception to the statement about equilibration of fluxes to within $<1\%$, as one of its grid cells exceeded the model’s temperature limit of 350 K during spin up while TOA fluxes were still 1.9% out of balance. Thus the results from that simulation are averaged over a period during which the planetary surface was still gradually heating, with a 2% TOA flux imbalance, instead of $<1\%$ like the others. Based on the behavior of the other simulations, the model would have warmed another 1–2 K in the mean if it had been able to run to equilibrium, a small error unlikely to have any impact on the qualitative trends demonstrated here.

2.2. Weathering Models

For both the **MAC** and the **WHAK** formulation, we calculate a weathering flux, F_{sil} (moles $\text{m}^{-2} \text{ yr}^{-1}$), in any grid cell that (i) has land, (ii) has a surface temperature above the triple point of water, 273.15 K, and (iii) has a local precipitation flux greater than zero. Here, we focus exclusively on continental silicate

weathering, ignoring the potential contribution of analogous reactions on the seafloor (e.g., Coogan & Gillis 2013) due to lack of clarity about the strength of this feedback, but we return to the issue of seafloor weathering in Section 5. A global weathering rate, W_{tot} (moles yr^{-1}), is calculated by multiplying each cell’s weathering flux by the surface area (dA) of the grid cell and then adding them all together, i.e.,

$$W_{\text{tot}} = \sum_{\text{lat,lon}} F_{\text{sil}} dA, \quad (2)$$

rendering the CO_2 consumption rate for a planet with the assumed weathering properties and background climate.

For silicate weathering to serve as a stabilizing negative feedback on planetary climate, it must act to maintain the climate at a set point determined by the properties of the silicates being weathered, the orbital and surface properties of the planet, and the planet’s CO_2 outgassing rate. This requires global weathering to accelerate with increases to $p\text{CO}_2$ and surface temperature. Under such conditions, if a planet has its climate perturbed in a way that makes its weathering rate fall below its CO_2 outgassing rate, CO_2 will be consumed more slowly than it is added to the atmosphere, leading to net CO_2 growth and surface warming until the global weathering rate has accelerated to the point that it is equal to outgassing, whence the atmospheric CO_2 content will stop evolving. In the opposite scenario, where global weathering decelerates in response to increases in $p\text{CO}_2$ and surface temperature, the process becomes a destabilizing feedback. In this case, the carbon/climate equilibrium where weathering matches outgassing is unstable. If $p\text{CO}_2$ is displaced to the high side of the equilibrium, weathering becomes less than outgassing, CO_2 would accumulate, and temperature would increase until something occurs to arrest the process (e.g., the planetary interior running out of CO_2). If $p\text{CO}_2$ is displaced to the low side of the equilibrium, weathering will exceed outgassing and $p\text{CO}_2$ will continue to decrease until a stable low- $p\text{CO}_2$ climate (possibly a snowball) is reached.

Thus the stability of a carbon cycle at a given instellation can be determined by calculating how the weathering rate changes with $p\text{CO}_2$ (the so-called “weathering curve”; Penman et al. 2020): If weathering rate is positively correlated with $p\text{CO}_2$, it acts as a stabilizing negative feedback, but if it is inversely correlated with $p\text{CO}_2$, it acts as a destabilizing positive feedback. So, rather than carry out very long asynchronously coupled simulations evolving atmospheric $p\text{CO}_2$ according to the balance between an assumed outgassing flux and a calculated weathering flux, we take the much simpler approach of doing a handful of simulations at a variety of $p\text{CO}_2$ and diagnosing the global weathering rates from these “snapshots.” Simply determining the sign of the slope of the weathering curve at a given instellation is sufficient for determining the stability of the carbon cycle. Under stabilizing conditions, imposing an outgassing rate would inexorably drive the $p\text{CO}_2$ to the level that generates a weathering rate equal to the assumed outgassing rate. Under destabilizing conditions, the final outcome would be determined by the initial conditions, i.e., whether the planet started off with outgassing greater than or smaller than its initial weathering rate.

In the next subsections, we describe how the two weathering models we deploy (**MAC** and **WHAK**) calculate F_{sil} as a function of local climate.

2.2.1. WHAK

The formulation of weathering developed in **WHAK** is the basis for the calculations in most previous exoplanet weathering/climate studies, including the few that have employed three-dimensional GCMs (e.g., Edson et al. 2012; Paradise & Menou 2017; Jansen et al. 2019; Paradise et al. 2019). We carry out calculations using the **WHAK** weathering formulation to compare with results from the **MAC** model, which is more closely tied to the underlying weathering chemistry than **WHAK**. **WHAK** weathering implicitly assumes silicate weathering rates are limited by the kinetics of silicate dissolution, which produces an exponential dependence on temperature. **WHAK** also includes a power-law dependence on CO₂ partial pressure ($p\text{CO}_2$). We represent this as

$$F_{\text{sil}} = \frac{W_{\text{ref}}}{\gamma_{\text{Earth}} \times 4\pi R_{\text{Earth}}^2} \times \exp\left(\frac{T - T_{\text{ref}}}{T_e}\right) \left(\frac{p\text{CO}_2}{p\text{CO}_{2,\text{ref}}}\right)^\beta, \quad (3)$$

where F_{sil} (mol m⁻² yr⁻¹) is the weathering flux from a grid cell, i.e., the number of divalent cations (which react with oceanic carbon to form carbonate minerals, ultimately removing CO₂ from the atmosphere) delivered to the ocean per unit time per unit land area in a given grid cell; W_{ref} is a reference global weathering rate (assumed equal to an estimate of Earth’s modern-day CO₂ outgassing; see Table 2); $\gamma_{\text{Earth}} \times 4\pi R_{\text{Earth}}^2$ is the approximate land area of the Earth, calculated by multiplying its land fraction (γ_{Earth}) by its surface area ($4\pi R_{\text{Earth}}^2$), necessary for translating W_{ref} from a global weathering rate into a weathering flux per unit land area; T (K) is the local surface temperature in a grid box; T_e is the e-folding temperature for the weathering reaction; $p\text{CO}_2$ (bar) is the CO₂ partial pressure; and β is the power-law dependence on $p\text{CO}_2$. The values of T_e and β , which determine the sensitivity of the reaction rate to changes in temperature and $p\text{CO}_2$, vary considerably for different silicate minerals. We choose the default values listed in Table 2 based on results from laboratory silicate dissolution experiments (e.g., Schott & Berner 1985; Brady 1991; Knauss et al. 1993; Oxburgh et al. 1994; Welch & Ullman 1996; Chen & Brantley 1998; Weissbart & Rimstidt 2000; Oelkers & Schott 2001; Palandri & Kharaka 2004; Carroll & Knauss 2005; Golubev et al. 2005; Bandstra & Brantley 2008; Brantley et al. 2008). In this formulation of **WHAK**, we ignore the runoff dependence assumed in the original formulation (Walker et al. 1981), as it has been demonstrated not to substantially impact global weathering rates, which are dominated by the exponential temperature dependence and power-law CO₂ dependence (Abbot et al. 2012). Further, truly kinetically limited weathering would not be impacted by changes to runoff, since the weathering rate would instead be determined by the rate of production of cations through silicate dissolution. Absent an accompanying change to temperature or $p\text{CO}_2$, any change to runoff above zero would simply change the dilution of weathering products without ultimately altering their rate of production or delivery to the ocean.

Table 2
Weathering Parameters Used in This Study.

Parameter	Units	Definition	Fiducial Value
γ_{Earth}	...	Earth’s land fraction	0.3
a_g	...	Surface albedo	0.05
R_{planet}	Meters (m)	Planetary radius	6.37×10^6
W_{ref}	Moles per year (mol yr ⁻¹)	Reference weathering rate equal to recent Earth outgassing estimate	3.4×10^{12} (Coogan & Gillis 2020)
T_{ref}	Kelvin (K)	Reference global-average temperature	288
$p\text{CO}_{2,\text{ref}}$	Bar	Reference CO ₂ partial pressure	280×10^{-6}
Λ	Variable	Thermodynamic coefficient for C_{eq}	1.4×10^{-3}
n	...	Thermodynamic $p\text{CO}_2$ dependence	0.316
α^*	...	$L\phi\rho_sAX_r\mu$ (see Section 2.2 and below)	3.39×10^5
$k_{\text{eff,ref}}^*$	Mol m ⁻² yr ⁻¹	Reference rate constant	8.7×10^{-6}
β	...	Kinetic weathering $p\text{CO}_2$ dependence	0.2 (Rimstidt et al. 2012)
T_e	K	Kinetic weathering temperature dependence	11.1 (Berner 1994)

Note. This table lists parameters used in our calculations, their units, their definitions, and the default values they take. A single asterisk (*) means the default parameter value was drawn from Table S1 of the supplement to Maher & Chamberlain (2014). For default parameters drawn from other sources, the citation is given in the “Value” column.

2.2.2. MAC

The other weathering model we apply in our simulations is modified from Graham & Pierrehumbert (2020), which applied a global-mean version of the **MAC** weathering model (Maher & Chamberlain 2014; Winnick & Maher 2018) to calculate global weathering fluxes from models of Earth-like exoplanets. The **MAC** model accounts for the impact of clay formation in the weathering zone, which sets a maximum concentration on weathering products in runoff, drastically increasing the importance of hydrology for determining weathering fluxes when water moves through the weathering zone at a rate that allows for weathering products to reach the maximum chemically equilibrated concentration. In this paper, rather than a global-mean formulation, we apply the weathering model from Graham & Pierrehumbert (2020) locally in each land grid cell, with the weathering flux in a given cell determined by the parameterized silicate properties, local H₂O precipitation flux, surface temperature, and $p\text{CO}_2$:

$$F_{\text{sil}} = \frac{\alpha}{[k_{\text{eff}}]^{-1} + mAt_s + \alpha[qC_{\text{eq}}]^{-1}}, \quad (4)$$

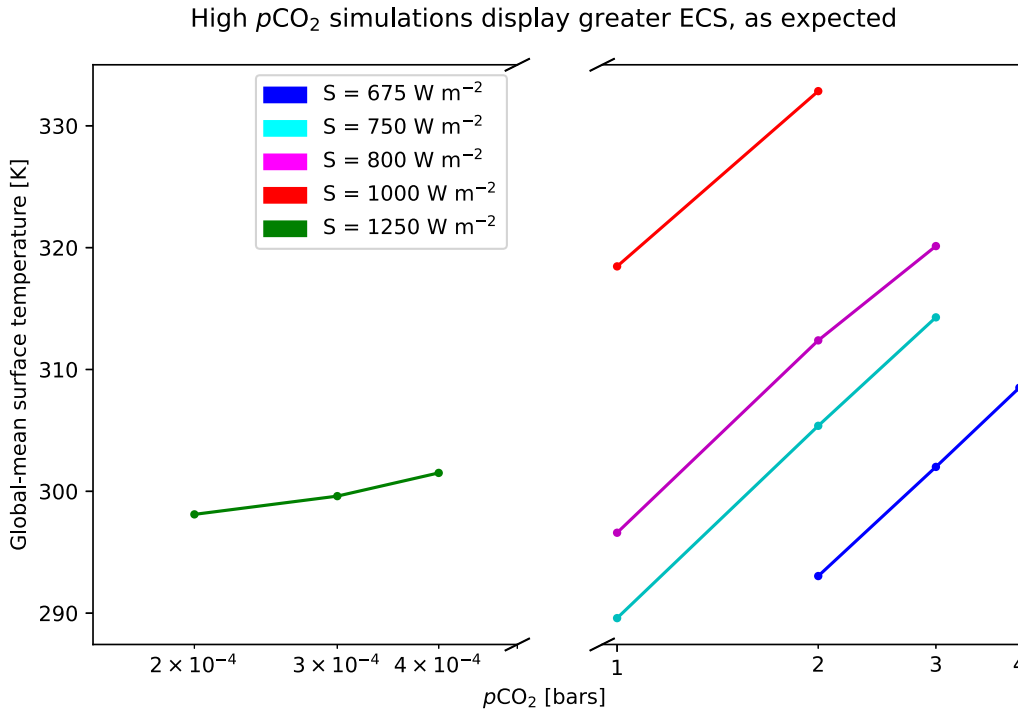


Figure 2. Global-mean surface temperature as a function of $p\text{CO}_2$ at various instellations S . The low- $p\text{CO}_2$, high-instellation simulations display an ECS of 3.4 K, close to estimates of the modern Earth’s (1.5–4.5 K). The high- $p\text{CO}_2$, low-instellation simulations all display ECS values of around 15 K due to CO_2 ’s self-broadening effect. Blue corresponds to $S = 675 \text{ W m}^{-2}$, cyan to 750 W m^{-2} , magenta to 800 W m^{-2} , red to 1000 W m^{-2} , and green to 1250 W m^{-2} .

where F_{sil} ($\text{mol m}^{-2} \text{ yr}^{-1}$) is the weathering flux from a given cell as above; α is a parameter that captures the effects of various weathering zone properties like characteristic water flow length scale, porosity, ratio of mineral mass to fluid volume, and the mass fraction of minerals in the weathering zone that are weatherable (see Graham & Pierrehumbert 2020 for a full explanation); $k_{\text{eff}} = k_{\text{eff, ref}} \exp\left(\frac{T_{\text{surf}} - T_{\text{surf, ref}}}{T_p}\right) \left(\frac{p\text{CO}_2}{p\text{CO}_2, \text{ref}}\right)^\beta$ ($\text{mol m}^{-2} \text{ yr}^{-1}$) is the effective kinetic weathering rate, i.e., the weathering rate in the absence of chemical equilibration with clay formation (Walker et al. 1981); m (kg mol^{-1}) is the average molar mass of minerals being weathered; A ($\text{m}^2 \text{ kg}^{-1}$) is the average specific surface area of the minerals being weathered; t_s (yr) is the mean age of the material being weathered; q (m yr^{-1}) is the flux of water through the grid cell, given by the precipitation in that grid cell output by the GCM; and $C_{\text{eq}} = \Lambda(p\text{CO}_2)^n$ (mol m^{-3}) is the maximum concentration of divalent cations in the water passing through weathering zones, as determined by chemical equilibrium between dissolving silicates and the secondary minerals (clays) that form from their products. The default values of all constants are given in Table 2.

By equating local precipitation and q , we are assuming that any rain that falls on land drives weathering that delivers solutes to the ocean, i.e., that all precipitation is converted to runoff. Thus these calculations provide an upper limit on weathering fluxes and the efficiency of MAC weathering as a climate feedback with a given set of parameters, as smaller rates of runoff to the ocean would reduce weathering rates. On modern Earth, 20%–26% of precipitation falling on land may be converted to runoff (Ghiggi et al. 2019; Graham & Pierrehumbert 2020; Coy 2022), but this value is likely to be heavily dependent on factors like topography, surface

temperature, and background atmosphere. As long as runoff is largely monotonic with precipitation, as seems likely (Le Hir et al. 2009; Ghiggi et al. 2019), (though it is unclear whether this must be the case O’Gorman et al. 2012), the qualitative behavior we describe should hold. Smaller rates of conversion from rain to runoff exacerbate the severity of the mechanism explored here by allowing the energetically limited regime to be accessed under smaller background CO_2 outgassing rates.

3. Results

3.1. Surface Temperature

The mean climate states and CO_2 equilibrium climate sensitivities (ECSs) of the simulations are in line with previously published estimates.

The ECS is the steady-state change in global-mean surface temperature from a doubling of atmospheric CO_2 , commonly used in studies of Earth’s climate (Knutti et al. 2017; Romps 2020; Goodwin 2021). The modern Earth’s ECS is generally estimated to fall between 1.5 K and 4.5 K per doubling (e.g., Knutti et al. 2017). This is consistent with the global-mean temperature behavior of our low- $p\text{CO}_2$ simulations, which warmed from 298.1 to 301.5 K as CO_2 was doubled from 200 to 400 ppmv (see green line and dots in Figure 2), indicating a reasonable ECS of 3.4 K. These simulations are substantially hotter than the modern Earth despite receiving 8% less TOA instellation because they lack clouds and the surface has a uniform, dark albedo of 0.05, resulting in planetary albedo of 0.1 due to N_2 ’s modest Rayleigh scattering effect, in contrast to Earth’s cloud- and ice-maintained albedo of 0.29 (Stephens et al. 2015). None of the low- $p\text{CO}_2$ simulations displays temperatures below freezing on any land mass, and in each case the fraction of planetary surface area below freezing at the

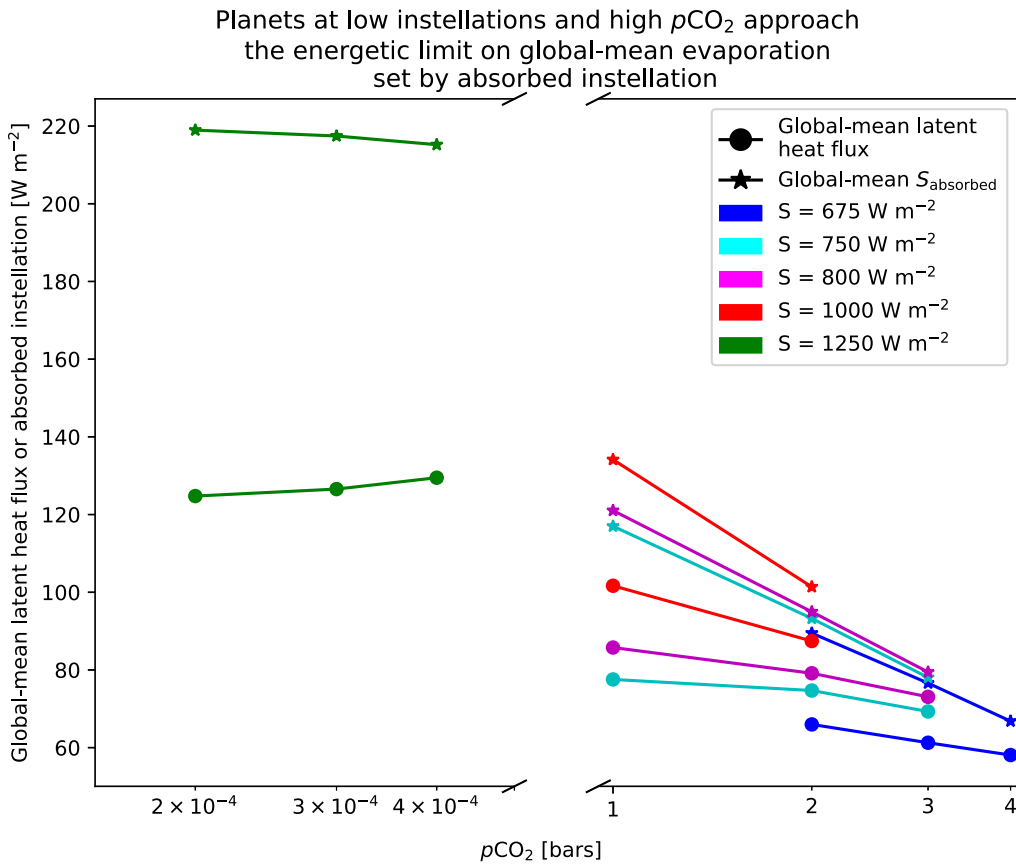


Figure 3. Global-mean absorbed instellation and global-mean upward latent heat flux as functions of $p\text{CO}_2$ at various S . For low- $p\text{CO}_2$, high-instellation simulations, latent heat flux (circle markers) increases with $p\text{CO}_2$, but remains far below absorbed instellation (star markers). For high- $p\text{CO}_2$, low-instellation simulations, a large majority of their absorbed instellation goes into the latent heat of evaporation. Colors are as in Figure 2.

poles is small (4.2%, 2.5%, and 1.7% for the 200 ppmv, 300 ppmv, and 400 ppmv simulations, respectively).

In climate simulations with very high CO_2 , ECS is known to increase as a function of $p\text{CO}_2$ due to the increasing importance of self-broadening and activation of spectral regions that are minor at lower pressures (e.g., Halevy et al. 2009; Pierrehumbert 2010; Russell et al. 2013; Wordsworth & Pierrehumbert 2013; Ramirez et al. 2014; Wolf et al. 2018; Graham 2021). Our high- $p\text{CO}_2$ simulations reflect this behavior, with all displaying an ECS of ≈ 15 K (see blue, cyan, magenta, and red lines with dots in Figure 2). This is consistent with the behavior of GCM simulations of early Earth atmospheres with instellations slightly larger and $p\text{CO}_2$ levels slightly lower than those presented here (Wolf et al. 2018), as well as with ECS values calculated using a polynomial fit (Kadoya & Tajika 2019) to radiative-convective column model output (Kopparapu et al. 2013) with 1 bar N_2 , saturated H_2O , and up to 10 bars CO_2 (Graham 2021). None of the presented high- $p\text{CO}_2$ simulations has temperatures below freezing on any land mass, and only the 1 bar, $S = 750 \text{ W m}^{-2}$ has any planetary surface area below freezing (5.2%, at the poles). Finally, as expected, with a given $p\text{CO}_2$, increased instellation leads to higher surface temperatures.

3.2. Energy Budgets and Precipitation

3.2.1. Low $p\text{CO}_2$, High Instellation

The behavior of the low- $p\text{CO}_2$ simulations is largely consistent with expectations from simulations of Earth's

climate. They approximately reproduce the expected positive trend in global-mean surface latent heat flux (green line with circle markers in Figure 3), the expected negative trend in global-mean upward long wave from the surface (green line with x-shaped markers in Figure 4), and the expected positive trend in precipitation (green lines in Figures 5 and 6). Averaged across the three low- $p\text{CO}_2$ simulations, global-mean latent heat flux and global-mean precipitation both increased by 1.1% K^{-1} , a bit less than the median value of 1.7% K^{-1} found in Earth climate simulations (Held & Soden 2006). Despite increasing somewhat with surface temperature, for all three low- $p\text{CO}_2$ simulations the latent heat flux remained far below the limit set by S_{abs} (green line with star markers in Figure 3), which decreased slightly in response to CO_2 's growth because of increased atmospheric absorption of instellation by H_2O as specific humidity rose. The total global-mean net upward long-wave flux decreased by 8.7 W m^{-2} from the 200 ppmv simulation to the 400 ppmv simulation, a somewhat greater reduction than the $4\text{--}5 \text{ W m}^{-2}$ per CO_2 doubling in Earth GCM simulations (e.g., Gutowski et al. 1991; Boer 1993), but this is to be expected since our low- $p\text{CO}_2$ simulations have a warmer background climate than Earth, meaning they should experience larger increases in highly opaque lower-tropospheric water vapor for a given change in temperature than cooler Earth simulations because of the exponential dependence of H_2O partial pressure on temperature. The sensible heat flux of the low- $p\text{CO}_2$ simulations changes very little as a function of CO_2 , with a reduction of $\approx 1 \text{ W m}^{-2}$ between the 200 and 300 ppmv simulations, and an increase of $\approx 1 \text{ W m}^{-2}$

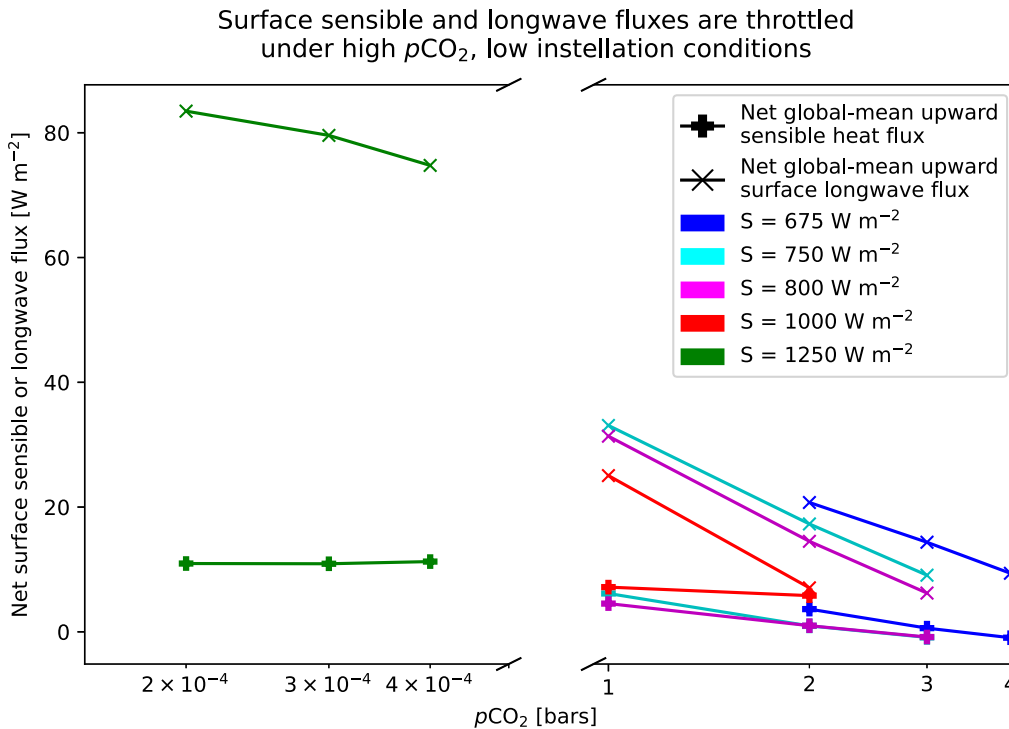


Figure 4. Net upward sensible or long-wave heat flux (W m^{-2}) as a function of $p\text{CO}_2$ for simulations at various S . For low- $p\text{CO}_2$ simulations, the sensible heat flux (x-shaped markers) changes little with $p\text{CO}_2$, while for high- $p\text{CO}_2$ simulations, it drops substantially, even becoming negative in some cases. For both low- and high- $p\text{CO}_2$ simulations, the long-wave flux (plus-shaped markers) decreases with increasing CO_2 , as expected. Colors are as in Figure 2.

between the 300 and 400 ppmv simulations (green line with plus-shaped markers in Figure 4). This contrasts slightly with simulations of Earth, where the surface’s upward sensible heat flux often decreases by $\approx 1 \text{ W m}^{-2}$ under a doubling of CO_2 (Gutowski et al. 1991; Boer 1993; Gómez-Leal et al. 2018), consistent across models with fixed sea surface temperatures, slab oceans (like ours), and fully coupled dynamical oceans (Myhre et al. 2017, 2018). This difference may be due to our neglect of topography, or it may be due to the fact that the climates we simulate are slightly warmer than modern Earth, biasing them toward smaller changes in sensible heat flux with surface temperature (Siler et al. 2019). Nonetheless, the changes in sensible heat flux are small in magnitude, and the flux itself is already a small enough term in the surface budget that it has no impact on our qualitative results.

3.2.2. High $p\text{CO}_2$, Low Instellation

The high- $p\text{CO}_2$, low-instellation simulations display markedly different behavior from those described above and are clearly operating in a regime where the energetic limit set by absorbed instellation exerts substantial influence. For all sets of high- $p\text{CO}_2$ simulations irradiated by a given S , global-mean upward latent heat flux at the surface decreases with increasing $p\text{CO}_2$, despite the fact that surface temperature increases substantially (see blue, cyan, magenta, and red lines with circles in Figure 3). These reductions in latent heat flux are accompanied (and driven) by large reductions in absorbed instellation at the surface (see blue, cyan, magenta, and red lines with stars in Figure 3) due mostly to increases in albedo from CO_2 ’s Rayleigh scattering, from values of 0.16–0.17 for the $p\text{CO}_2 = 1$ bar cases, to 0.26–0.27 in the $p\text{CO}_2 = 3$ bars simulations, to 0.30 in the $p\text{CO}_2 = 4$ bars case, consistent with previous simulations of planets with extremely high $p\text{CO}_2$

Table 3
Fraction of Absorbed Instellation Going into Evaporation $\frac{L}{S_{\text{abs}}}$.

	S (W m^{-2})				
	675	750	800	1000	1250
$p\text{CO}_2$ (bars)
2×10^{-4}	0.57
3×10^{-4}	0.58
4×10^{-4}	0.60
1	...	0.66	0.71	0.76	...
2	0.74	0.80	0.83	0.86	...
3	0.80	0.89	0.92
4	0.87

Note. Table layout identical to Table 1 except $\frac{L}{S_{\text{abs}}}$ values replace checkmarks.

(Kasting & Ackerman 1986; Ramirez et al. 2014). As $p\text{CO}_2$ is increased in these simulations, even though the absolute latent heat flux goes down an increasing proportion of the absorbed instellation at the surface goes into evaporation, with values ranging from 66% to 92% for the high- $p\text{CO}_2$ cases, compared with a range of 57%–60% for the low- $p\text{CO}_2$ simulations (see Table 3). Correspondingly, the sensible and long-wave heat flux contributions to the surface energy budgets in the high- $p\text{CO}_2$ simulations are substantially reduced in both absolute and relative terms (see blue, cyan, magenta, and red plus-shaped markers and x-shaped markers in Figure 4). Interestingly, the global-mean sensible heat flux becomes negative (directed into the surface) in the $p\text{CO}_2 = 3$ bars simulations irradiated by $S = 750 \text{ W m}^{-2}$ and 800 W m^{-2} and in the $p\text{CO}_2 = 4$ bars, $S = 675 \text{ W m}^{-2}$ simulation, but in each case the net sensible heating of the surface is less than 1 W m^{-2} .

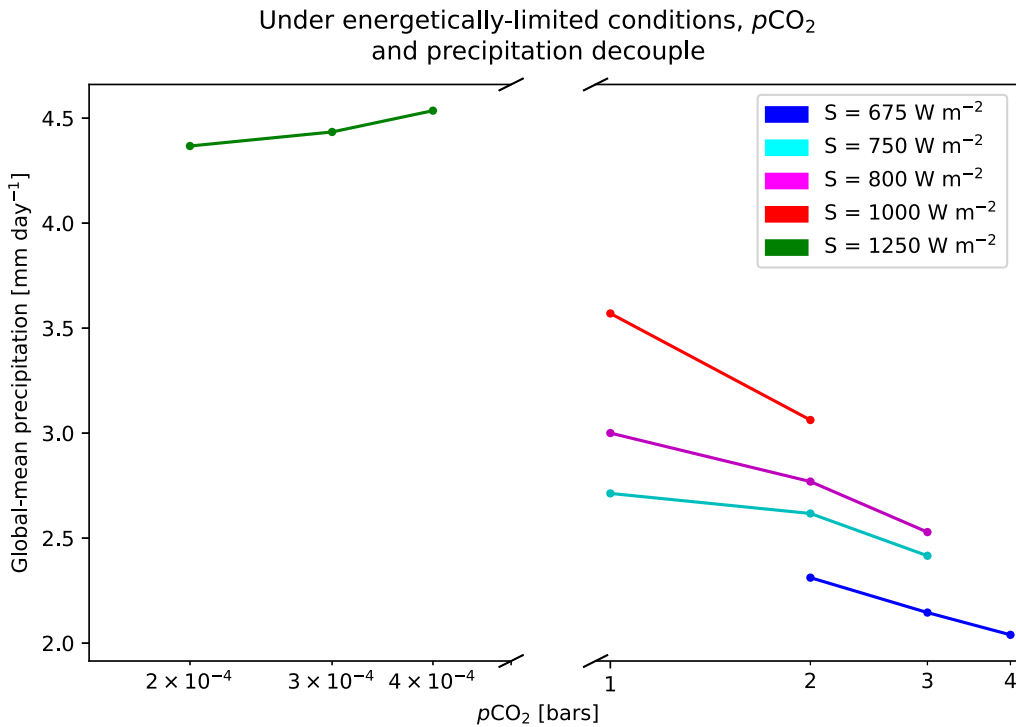


Figure 5. $p\text{CO}_2$ vs. global-mean precipitation. For low- $p\text{CO}_2$, high-instellation simulations, precipitation increases with $p\text{CO}_2$. For high- $p\text{CO}_2$, low-instellation simulations in the regime where a large majority of their absorbed instellation goes into driving evaporation, precipitation falls with $p\text{CO}_2$. Colors are as in Figure 2.

As implied by the trends in latent heat flux versus $p\text{CO}_2$ displayed in Figure 3, global-mean precipitation rates in the high- $p\text{CO}_2$ simulations fall with increasing CO_2 (see blue, cyan, magenta, and red lines in Figure 5). This results in counterintuitive behavior, driving precipitation rates that decrease with increasing surface temperature (see blue, cyan, magenta, and red lines in Figure 6). Despite some high- $p\text{CO}_2$ simulations having surface temperatures much larger than the low- $p\text{CO}_2$ simulations, the low- $p\text{CO}_2$ simulations all have global-mean precipitation rates larger than any of the high- $p\text{CO}_2$ simulations, consistent with the fact that the low- $p\text{CO}_2$ precipitation rates are sustained by latent heat fluxes larger than the S_{abs} received by any of the high- $p\text{CO}_2$ simulations except the $p\text{CO}_2=1$ bar, $S=1000 \text{ W m}^{-2}$ case (compare green line with circles to blue, cyan, magenta, and red lines with stars in Figure 3). In the next section, we explore the implications of this energetically limited precipitation behavior for the functioning of the carbon cycle.

3.3. Weathering Rates

In this section, we will present estimates of weathering rates based on output fields from the GCM simulations described above, with weathering fluxes calculated according to both the WHAK and MAC formulations. Sensitivity tests varying the parameters in the weathering models within plausible ranges generated fairly large changes in absolute fluxes, but did not affect the qualitative picture presented here.

3.3.1. WHAK Weathering

When weathering is calculated according to the WHAK formulation (Equation (3)), the weathering rate increases strongly in response to increases in $p\text{CO}_2$ and S for all simulations, regardless of initial $p\text{CO}_2$ or instellation (see Figure 7). This makes sense, given the WHAK formulation’s

exponential temperature dependence and power-law $p\text{CO}_2$ dependence, both of which naturally produce big increases in weathering fluxes for modest changes in temperature and/or $p\text{CO}_2$. The increases produced by this model are unrealistically large even if we take the WHAK formulation at face value, as the global rate of rock uplift sets a “supply limit” on the rate of silicate weathering of $\mathcal{O}(100)$ trillion moles of CO_2 per year on Earth (Tmol yr^{-1}) (e.g., Kump 2018), but the positive slope of the curves in Figure 7 confirms in principle the continued operation of WHAK weathering as a negative feedback even under high- $p\text{CO}_2$, low-instellation conditions where energetically limited precipitation is relevant. Earth’s outgassing rate is generally estimated to lie somewhere between 3 and 15 Tmol yr^{-1} (Coogan & Gillis 2020), substantially smaller than even the smallest weathering rate produced by these simulations, but this is due to our mostly arbitrary choice of weathering constant W_{ref} in Equation (3). A smaller W_{ref} would produce proportionally smaller weathering rates without changing the qualitative trends in weathering versus $p\text{CO}_2$.

3.3.2. MAC Weathering

With MAC weathering, the low- $p\text{CO}_2$ simulations respond essentially as expected (Figure 8). Although the strength of the weathering response to the changes in the surface climate is much weaker than in the WHAK case, the weathering rate in the low- $p\text{CO}_2$ simulations still increases with increasing $p\text{CO}_2$, producing a stabilizing negative feedback. This provides tentative evidence that MAC-style continental weathering may be able to stabilize the climates of planets under Earth-like conditions of high instellation and low $p\text{CO}_2$.

In contrast, the high- $p\text{CO}_2$, low-instellation simulations in the energetically limited regime produce a drastically different carbon cycle than the WHAK calculations or the low- $p\text{CO}_2$ MAC calculations would suggest. While they do display

Under energetically-limited conditions,
global-mean surface temperature
and precipitation decouple

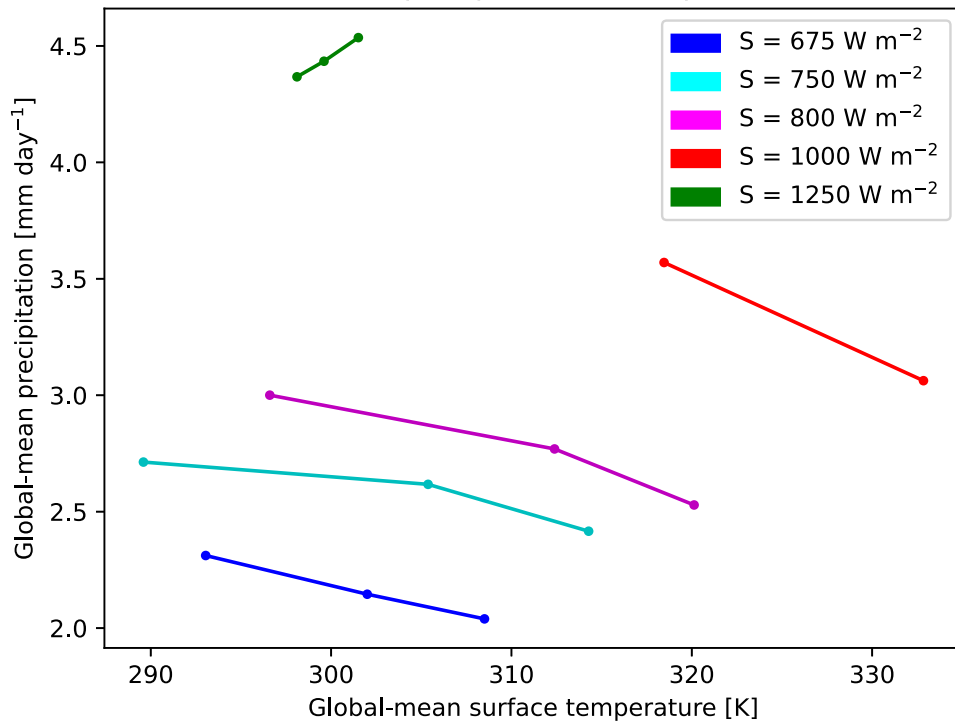


Figure 6. Global-mean surface temperature vs. global-mean precipitation. For low- $p\text{CO}_2$, high-instellation simulations, precipitation increases with surface temperature. For high- $p\text{CO}_2$, low-instellation simulations in the regime where a large majority of their absorbed instellation goes into driving evaporation, precipitation falls with temperature. Colors are as in Figure 2.

WHAK weathering increases rapidly with $p\text{CO}_2$
despite sluggish hydrology

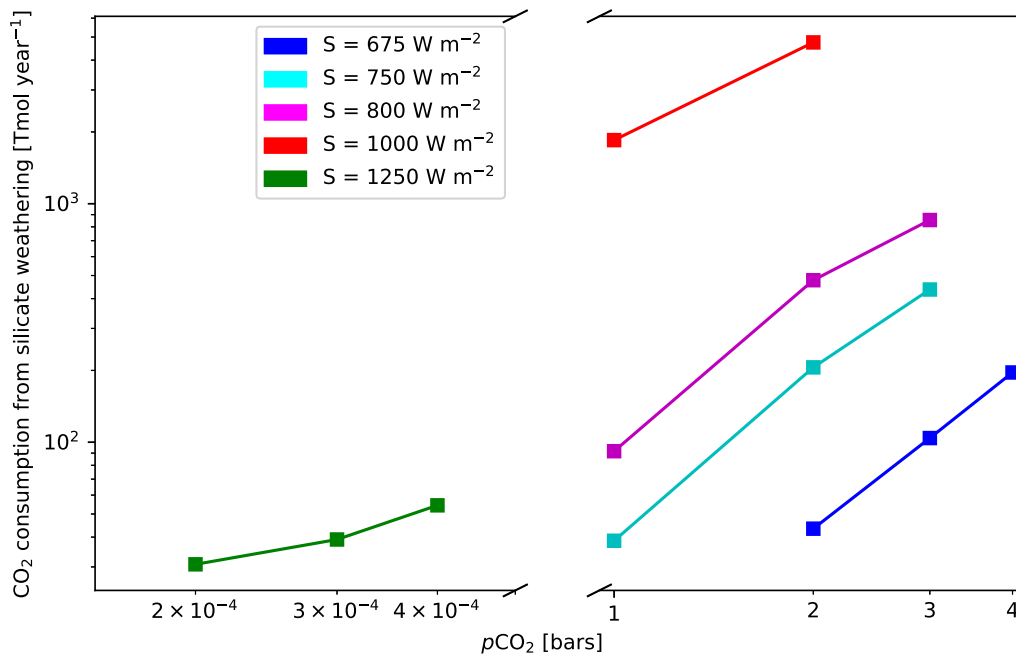


Figure 7. Global WHAK weathering rates (Tmol yr^{-1}) vs. $p\text{CO}_2$ for a variety of instellations. Weathering fluxes are calculated according to the WHAK formulation (Equation (3)). For all simulations, the weathering rate increases with CO_2 . Colors are as in Figure 2.

somewhat higher weathering rates than the low- $p\text{CO}_2$ simulations due to the thermodynamic $p\text{CO}_2$ dependence of the maximum concentration of weathering products in runoff

(C_{eq} in Equation (4), a much weaker effect than that of the $p\text{CO}_2$ dependence of WHAK weathering represented by β in Equation (3)), all of the high- $p\text{CO}_2$ simulations display the

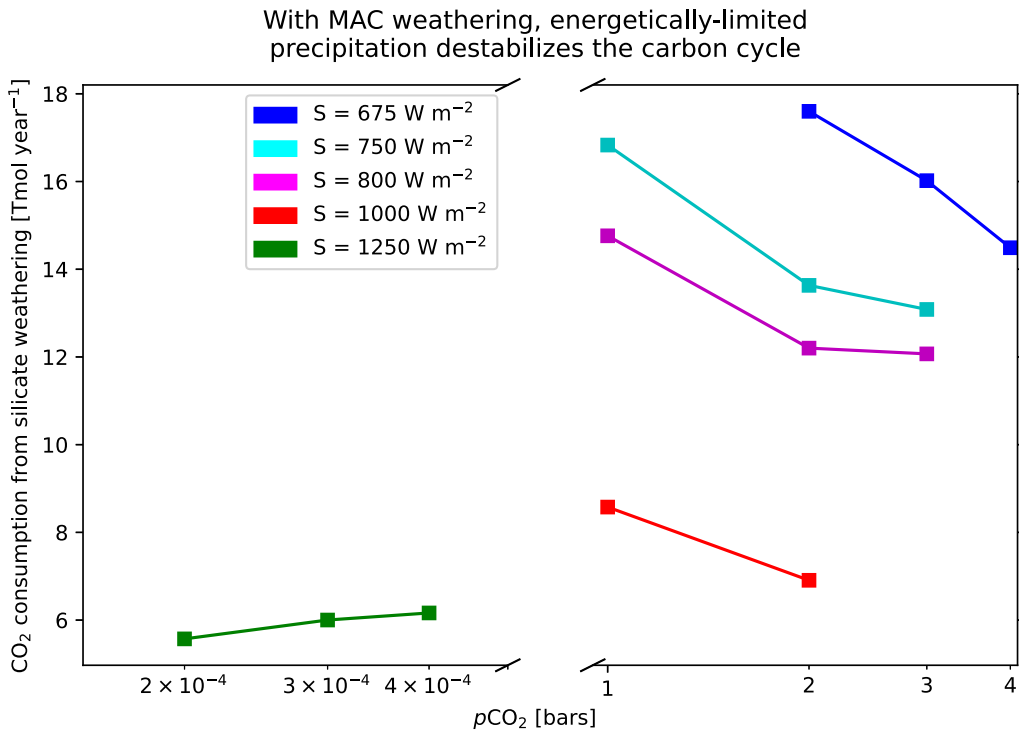


Figure 8. Global MAC weathering rates with fiducial parameter values (Tmol yr^{-1}) vs. $p\text{CO}_2$ for a variety of instellations. Weathering fluxes are calculated according to the MAC formulation (Equation (4)). For low- $p\text{CO}_2$ simulations, the weathering rate increases with CO_2 , while for high- $p\text{CO}_2$ simulations, weathering decreases with increasing CO_2 . Colors are as in Figure 2.

opposite response to further increases in CO_2 : At a given S , as $p\text{CO}_2$ increases (along with surface temperature), the global weathering rate goes down (see blue, cyan, magenta, and red lines in Figure 8). As described in Section 2.2, anticorrelation between global weathering rates and $p\text{CO}_2$ destabilizes the carbon cycle, so the high- $p\text{CO}_2$ simulations are all displaying a defective climate thermostat with a positive feedback that would likely induce runaway climate heating or cooling. Although this result runs counter to Earth-based intuitions, the unusual trends in $p\text{CO}_2$ versus weathering make sense given the increased importance of hydrologic cycling in the MAC weathering framework and the reduction in global-mean precipitation triggered by reduced S_{abs} .

Another unexpected weathering trend appears in the set of high- $p\text{CO}_2$ simulations: Holding CO_2 constant, the global weathering rate goes down even as instellation rises and drives both surface temperature (Figure 2) and global-mean precipitation (Figure 5) upward with it. This trend obviously cannot be explained by a global-mean argument, since all of the variables that directly control weathering are, in bulk, either increasing (i.e., q and surface temperature) or staying the same (i.e., $p\text{CO}_2$) as S is increased. Instead, the explanation lies in the intensification of moisture extremes expected in warming climates from simple thermodynamic considerations (Held & Soden 2006; Allan et al. 2020), often referred to by the phrase “wet gets wetter, dry gets drier” (WGWDGD) in discussions of Earth’s climate (Allan et al. 2020), though over the past several years it has become clear that this basic picture does not hold as well over land in Earth simulations as it does over the ocean (Byrne & O’Gorman 2015; Feng & Zhang 2015; Allan et al. 2020). Although WGWDGD does not perfectly describe the moisture response over land in Earth simulations under the (comparatively) small climate perturbations projected for this

century, it quite accurately describes the behavior of the precipitation in our high- $p\text{CO}_2$ simulations as S is increased.

In other words, although the total global precipitation flux increases with S in our high- $p\text{CO}_2$ simulations, it also becomes concentrated onto a smaller area, meaning deserts expand as S goes up. For example, in the $S = 675 \text{ W m}^{-2}$, $p\text{CO}_2 = 2$ bars case, over half of the planet’s land area receives more than 1 mm day^{-1} precipitation, whereas only about a quarter of the land area in $S = 1000 \text{ W m}^{-2}$ receives that much water (see right side of Figure 9). This is compensated by an increasing fraction of land mass with high precipitation fluxes, i.e., only $\approx 5\%$ of the land mass in the aforementioned $S = 675 \text{ W m}^{-2}$ simulation exceeds 4 mm day^{-1} of rain, but about 20% of the land mass in the 1000 W m^{-2} simulation meets that criterion, and higher S generally leads to a longer “tail” of land mass with large local precipitation fluxes. As can be seen by comparing the weathering flux curves on the left side of Figure 9 with the precipitation flux curves on the right, local weathering tracks local precipitation quite directly, so it might seem that the long tail of high precipitation over land should more than make up for the expansion in dry areas. However, past a point determined by balance between the kinetics of silicate dissolution and the timescale and surface area of contact between water and dissolving silicates, extremely high precipitation has diminishing returns in terms of weathering rates (Maher & Chamberlain 2014). If water flushes out a weathering zone rapidly enough, the system becomes kinetically limited and any further increases to the water’s flow rate will simply change the degree of dilution of weathering products rather than increasing their flux. We can see this effect in Figure 9, where all of the local weathering fluxes drop off abruptly around $0.2 \text{ mol m}^{-2} \text{ yr}$ even though a direct scaling of weathering flux with water flux would suggest a long tail of much larger local fluxes for the $S = 1000 \text{ W m}^{-2}$

Expanding deserts can reduce silicate weathering under increasing instellation

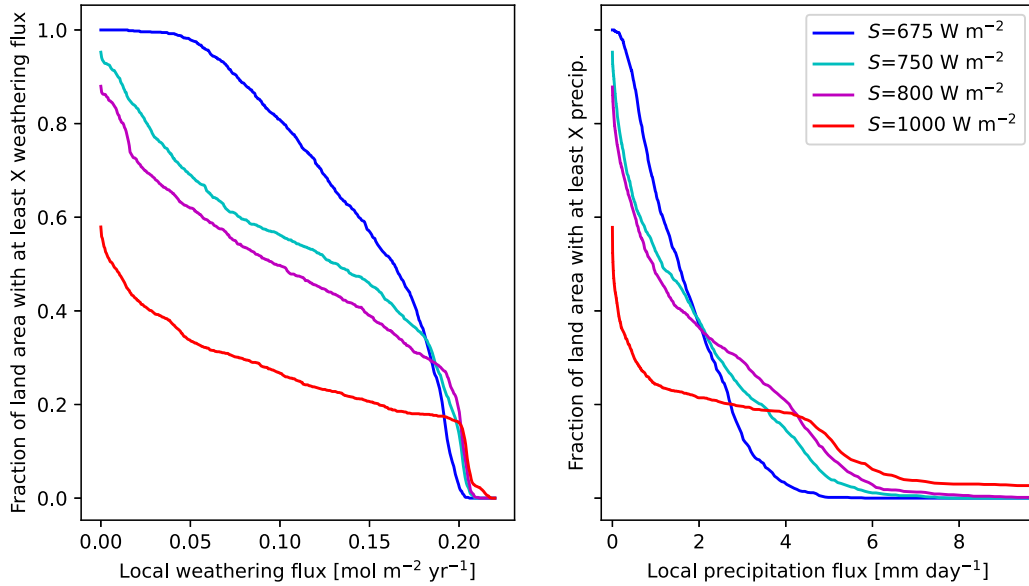


Figure 9. The change in spatial distribution of MAC weathering (left) and precipitation (right) that accompanies increasing TOA instellation. Results shown are for simulations with $p\text{CO}_2 = 2$ bars and $S = 675 \text{ W m}^{-2}$ (blue), $S = 750 \text{ W m}^{-2}$ (cyan), $S = 800 \text{ W m}^{-2}$ (magenta), and $S = 1000 \text{ W m}^{-2}$ (red). The y-value of a curve represents the fraction of land with at least as much weathering flux (left) or precipitation (right) as the corresponding x-axis value. Even though the total global precipitation increases as S increases, the total global weathering rate decreases because less land is receiving substantial precipitation. See Section 3.3. Colors are as in Figure 2.

simulation. Interestingly, although the precipitation rate and S_{abs} both increase as S goes up, simulations at a given $p\text{CO}_2$ still move progressively closer to the energetic limit set by S_{abs} (see Table 3), which may play a role in constraining the areal extent of precipitation over land and forcing the growth of desert regions. The potential for reduction in weathering with increased S is another destabilizing influence in the carbon cycle, since even with a functional negative feedback at a given instellation (i.e., positive slope in weathering versus $p\text{CO}_2$), this effect would force $p\text{CO}_2$ to higher equilibria at higher installations, likely significantly reducing a planet’s habitable lifetime under increasing host-star luminosity.

4. Discussion

4.1. Catastrophic Carbon Cycle Hysteresis

With MAC-style, hydrologically regulated weathering, energetically limited precipitation can cause a breakdown of the negative feedback on climate that emerges within the carbonate-silicate cycle. Our high- $p\text{CO}_2$, low-instellation simulations displayed reductions in weathering with CO_2 growth, opposite the trend required to stabilize climate by balancing CO_2 sequestration against CO_2 outgassing. This implies that in the portion of the instellation- CO_2 space we have probed, which are generally characteristic of the outer reaches of the conventional HZ, coupled climate/carbon cycle equilibria are unstable. The instability is not just a local instability to infinitesimal displacements. The unstable equilibria represent the attractor basin boundary between low- CO_2 states when the system is displaced on the cold side, and states with very high CO_2 when the system is displaced on the warm side. The unstable branch extends over the entire range of CO_2 for which weathering decreases with CO_2 . For each instellation considered, weathering decreases with increasing CO_2 in the high- CO_2 regime. However, in the colder low- CO_2 regime,

weathering is expected to increase with CO_2 because precipitation is not subject to an energy limit. (We have demonstrated that explicitly only for one instellation value). Based on these two end-member behaviors, it is inferred that there is a maximum weathering rate which, for the lower ranges of instellation we have considered, occurs at a $p\text{CO}_2$ somewhere below 1 bar.

The inferred structure of the weathering curve governing climate/carbon equilibrium is shown schematically in Figure 10, assuming there to be only one local maximum of weathering. The value of $p\text{CO}_2$ at which peak weathering occurs and the height of the peak depend on instellation. Our simulations have probed just a portion of the relevant instellation space, and only a portion of the right-hand half of the curve where weathering decreases with $p\text{CO}_2$. In particular, we have not located the peak of the weathering curve, which occurs in the gap between our low- and high- $p\text{CO}_2$ simulations. The geometry of the weathering curve indicates the presence of a saddle-node bifurcation (e.g., Strogatz 1994) in the climate/carbon equilibrium. For a given volcanic outgassing rate below peak weathering (indicated by the horizontal line labeled “V” in the figure), there are two equilibria. The equilibrium P_2 to the right is unstable: this is the unstable high- $p\text{CO}_2$ equilibrium we have identified in our simulations. If the system initially has $p\text{CO}_2$ anywhere to the left of P_2 , it will be attracted to the stable low- $p\text{CO}_2$ equilibrium P_1 . Because our simulations have not located the peak, we cannot determine whether the stable state P_1 is a snowball or a habitable low- $p\text{CO}_2$ state with above-freezing conditions.

If the system starts somewhat to the right of P_2 , then CO_2 will accumulate until something arrests the process at higher $p\text{CO}_2$. This could terminate at complete degassing of the interior CO_2 reservoir, leading to a hot Venus-like state with a thick gaseous atmosphere or a more temperate state where CO_2 accumulates in the form of a liquid ocean, depending on

Energetically-limited precipitation introduces bifurcation and hysteresis into the carbon cycle

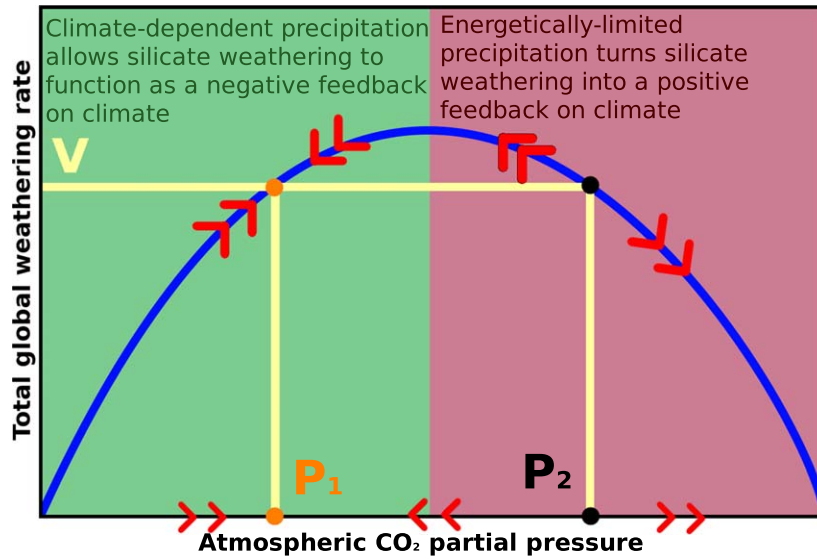


Figure 10. A schematic of the saddle-node bifurcation in the carbon cycle suggested by our simulations. The blue curve represents the global weathering rate as a function of $p\text{CO}_2$. Weathering increases with increasing $p\text{CO}_2$ (and surface temperature) in the green zone, and it decreases with increasing $p\text{CO}_2$ (and surface temperature) in the red zone. Weathering rates are equal to outgassing (V) at $p\text{CO}_2 = P_1$ (orange) and at $p\text{CO}_2 = P_2$ (black). The P_1 equilibrium is stable because weathering acts as a negative feedback in that regime, while the P_2 equilibrium is unstable due to silicate weathering’s positive-feedback behavior. The red arrows indicate the directions CO_2 and weathering would evolve for a climate initialized from various points relative to the two equilibria.

installation as in Graham et al. (2022). Alternatively, it is possible that the weathering curve turns around at sufficiently high $p\text{CO}_2$, allowing a new stable high- $p\text{CO}_2$ equilibrium to exist, though possibly at an uninhabitably hot temperature. Because the processes leading to the decrease of weathering with $p\text{CO}_2$ persist and even accentuate at higher values than we have probed, we think this unlikely, but it is a possibility that cannot be ruled out at present. In any event, the unstable-equilibrium P_2 is a basin boundary between stable low- and high- $p\text{CO}_2$ states.

It is generic to the geometry of saddle-node bifurcations that the system supports hysteresis. Suppose the planet starts in the stable equilibrium P_1 at a time when volcanic outgassing is relatively weak. If outgassing increases subsequently, and exceeds the peak of the weathering curve, then the system will transition to a stable high- $p\text{CO}_2$ equilibrium somewhere past the right edge of the diagram. Because any state to the right of P_2 will be attracted to the high- $p\text{CO}_2$ state, volcanic outgassing would need to be reduced to below its original value in order to restore a stable low- $p\text{CO}_2$ state. Because the peak of the weathering curve depends on instellation, it is also possible for such hysteresis loops to occur for fixed outgassing, as a result of evolution of stellar luminosity. Our simulations indicate that increasing instellation in the high- $p\text{CO}_2$ states decreases weathering, and so likely reduces the peak weathering. This scenario could lead to a new form of habitability termination as a G or F star increases in luminosity over its main-sequence lifetime.

There are additional pathways into the energetically limited regime that do not require any changes to outgassing or instellation. For example, if the $p\text{CO}_2$ necessary to deglaciate a planet in a snowball state lies at $p\text{CO}_2 > P_2$ (black markers in Figure 10), then escape from global glaciation due to reduced weathering in icy conditions could counterintuitively propel a previously temperate planet into a death spiral of uncontrolled

heating. Upon accumulating enough CO_2 to deglaciate, rather than weathering away the excess to return to a temperate climate, runaway CO_2 accumulation would ensue due to the processes described above for planets initialized from $p\text{CO}_2 > P_2$. Similarly, if Earth-like planets outgas massive CO_2 atmospheres during their magma-ocean phases like some models suggest (e.g., Solomatova & Caracas 2021), some may become “locked in” to this early, hot, high- $p\text{CO}_2$ phase, since their weathering rates after magma-ocean crystallization and water-ocean condensation might remain pinned below their early outgassing rates due to energetically constrained precipitation. However, expectations that planets will also face a large flux of impacts producing highly weatherable ejecta in the early stages after planet formation (e.g., Kadoya et al. 2020) may help mitigate this danger. Further, at low instellations deglaciation can be prevented by CO_2 condensation onto the icy planetary surface (Turbet et al. 2017; Kadoya & Tajika 2019), which may restrict the parameter space that allows for a post-snowball death spiral.

A more quantitative example of how CO_2 runaway might play out can be illustrated with direct reference to Figure 8. The $p\text{CO}_2 = 1$ bar, $S = 1000 \text{ W m}^{-2}$ simulation (red squares in Figure 8) displays a weathering rate of 8.6 Tmol yr^{-1} . If we take this as our initial climate state and impose a volcanic CO_2 degassing rate of 10 Tmol yr^{-1} , which is well within the range of estimates for Earth’s outgassing rate (Catling & Kasting 2017; Coogan & Gillis 2020), the planet’s $p\text{CO}_2$ will begin to grow because the flux into the atmosphere is greater than the flux out. Under Earth-like conditions, this would cause warming, an intensification of the hydrological cycle, and an acceleration in weathering (as we see in the low- $p\text{CO}_2$ cases, the green squares in Figure 8), moving the carbon cycle closer to equilibrium; but in this case the opposite happens, with a progressive reduction in the weathering rate as CO_2 accumulates. By the time our hypothetical $S = 1000 \text{ W m}^{-2}$

planet had accumulated another bar of CO_2 , its weathering rate would have fallen to only 6.9 Tmol yr^{-1} (see red square at $p\text{CO}_2 = 2$ bars in Figure 8). Thus the planet would have a carbon cycle further out of balance with its 10 Tmol yr^{-1} outgassing rate than when it started, with no signs of slowing down. We did not carry the $S = 1000 \text{ W m}^{-2}$ simulations to higher $p\text{CO}_2$ because of the temperature constraints of our modeling framework, but even at $p\text{CO}_2 = 2$ bars the planet is verging on inhospitable conditions, with a global-mean surface temperature in excess of 330 K (red dot at $p\text{CO}_2 = 2$ bars in Figure 2). Assuming the negative weathering trend holds out to even larger $p\text{CO}_2$, or at least that the weathering rate remains below the assumed 10 Tmol yr^{-1} outgassing rate, the planet would eventually be forced by the carbonate-silicate cycle into an uninhabitably hot state, likely continuing to warm until it degassed all of the available CO_2 from its interior, ending up with a dense, steamy, supercritical $\text{CO}_2/\text{H}_2\text{O}$ atmosphere unless some unknown process was triggered along the way that allowed the weathering rate to accelerate back to parity with the outgassing rate. Simulations of water photolysis and hydrogen escape on CO_2 -rich planets orbiting G stars suggest that the upper-atmospheric cold trap generated by the low instellations and high- CO_2 partial pressures under consideration would throttle water loss to insignificant levels, allowing these hot, steam-rich surface conditions to persist over geologic time-scales (Wordsworth & Pierrehumbert 2013).

At somewhat lower instellations than $S = 1000 \text{ W m}^{-2}$, CO_2 condensation at the surface would become a possibility at high enough $p\text{CO}_2$, meaning the energetic limit on precipitation presents a pathway to reach the stable CO_2 ocean states proposed in Graham et al. (2022). The mechanism of carbon cycle destabilization suggested in that study was based on the fact that CO_2 becomes a coolant at extremely high partial pressures, which also leads to a slowdown of weathering with $p\text{CO}_2$ accumulation but requires much higher CO_2 to initiate than the mechanism discussed here. This means that energetically limited weathering may increase the probability that low-instellation planets within the HZ end up with CO_2 oceans, with uncertain implications for their habitability. Although CO_2 ocean worlds are restricted to relatively clement climates below 304 K (the critical temperature of CO_2), they would still sport extreme surface pressures (up to 72 bars), and in the process of accumulating that much CO_2 surface temperatures can peak at extreme levels ($>400 \text{ K}$) before Rayleigh scattering begins to outweigh CO_2 's greenhouse effect and further accumulation begins to cool the planet (Graham et al. 2022). Intriguingly, some work has suggested that liquid and supercritical CO_2 may be conducive to prebiotic chemistry (Shibuya & Takai 2022), and supercritical CO_2 may drive rapid carbonate formation (see Section 5 and McGrail et al. 2017), suggesting these worlds may not be as hostile to life as they appear at first.

4.2. Limit Cycling?

First, we note that our Walker et al. 1981 weathering results (Figure 7) are qualitatively consistent with previous WHAK-based exoplanet weathering calculations driven by zero-dimensional (Menou 2015; Abbot 2016), one-dimensional (Haqq-Misra et al. 2016; Kadoya & Tajika 2019), and three-dimensional (Paradise & Menou 2017) climate models. In all of these cases, the direct power-law dependence of weathering fluxes on $p\text{CO}_2$ (the β term in Equation (3)) means that planets

at lower instellations (where larger $p\text{CO}_2$ is necessary to maintain a given surface temperature) display much higher weathering rates under temperate conditions, necessitating colder surface climates to reduce weathering enough to equilibrate with an Earth-like outgassing rate. Under fairly broad combinations of instellation and weathering properties (e.g., Abbot 2016), this direct $p\text{CO}_2$ dependence was suggested to draw CO_2 down to levels that would glaciare planets. This led to the prediction that terrestrial planets in the outer reaches of the HZ would spend most of their time in snowball states, punctuated by intermittent periods of temperate surface conditions when cold- and ice-induced slowdowns in weathering allowed CO_2 to build up to high enough levels to achieve deglaciation briefly, at which point weathering would accelerate again and reglaciate the planet, a periodic process termed “limit cycling” (Menou 2015; Haqq-Misra et al. 2016). The huge increases in WHAK weathering rates for our high- $p\text{CO}_2$ simulations (Figure 7) are consistent with this picture, though we did not carry out simulations at low enough $p\text{CO}_2$ values and surface temperatures to determine whether the WHAK weathering rates would remain extremely high even as the planets approached glaciare.

Compared to the results discussed above, our MAC weathering calculations (see Figure 8) suggest completely different behavior for planets with CO_2 -dominated atmospheres at reduced instellations within the HZ. Although they do display somewhat higher weathering rates than their low- $p\text{CO}_2$ counterparts because of the $p\text{CO}_2$ dependence of the equilibrium concentration of solutes (C_{eq} in Equation (4)), the high- $p\text{CO}_2$ MAC simulations do not display the orders-of-magnitude increase in weathering compared to cases with lower CO_2 that is seen with WHAK. From this, it seems that MAC weathering imparts much less susceptibility to the limit-cycling mechanism, which at first glance appears to be a point in favor of climate stability at low instellation. However, the carbon cycle instability discussed in Section 4.1, which sets in under low-instellation and high- CO_2 conditions when using MAC weathering, has the potential to pose an equal or greater threat to habitability in the outer portions of the conventional HZ. Unlike climate limit cycling, this instability does not depend on glaciare, though the cold-side attractor could in some cases be a snowball state. In such cases, the CO_2 buildup required to trigger deglaciation could be large enough to flip the system into the hot-side high- CO_2 attractor. Since we have not quantified the hot-side attractor, we have no basis at present to speculate as to whether there are mechanisms that could return the system to a snowball state and thus lead to a form of climate limit cycling.

The novel carbon cycle instability our work has identified suggests mechanisms whereby the geochemical HZ could be significantly contracted relative to the conventional HZ, which does not take into account geochemical constraints. The extent to which habitability in the outer portions of the conventional HZ is actually threatened is subject, however, to the resolution of a number of caveats.

5. Caveats

In this study, we focused exclusively on modeling continental silicate weathering rates in a significantly simplified cloud-free GCM with a specific, idealized land configuration and an assumption of spatially uniform lithology and soil properties. There are a variety of possibilities that we did not

model which could prevent or complicate the carbon cycle destabilization discussed above.

5.1. *Mind the Gap*

The most important limitation in the results presented above is the gap between our low- $p\text{CO}_2$ simulations and our high- $p\text{CO}_2$ simulations. This gap was due to technical issues with finding a computationally feasible spectral representation that would enable the radiation code to cover the whole range. Filling in the gap also would require incorporation of ice-albedo feedback, and probably also dynamic ocean effects, in order to resolve the snowball transition properly.

For our lowest-irradiation case, 675 W m^{-2} , one-dimensional calculations indicate that $p\text{CO}_2$ in excess of 1 bar would be necessary to keep the global-mean surface temperature above freezing (Figure 6 Koppapu 2013). Our simulations did not probe below 2 bars for this irradiation, but at 2 bars the weathering still is strongly increasing as $p\text{CO}_2$ decreases, so it is likely that the unstable feedback continues to 1 bar and below. For this case, at least, it seems plausible that the low- $p\text{CO}_2$ attractor is a snowball. For the higher irradiances in our simulations, the actual position of the peak weathering becomes crucial to the question of whether the attractor is a snowball.

Our suite of simulations also has a gap for $p\text{CO}_2$ above 4 bars, so we cannot say where the $p\text{CO}_2$ and temperature ultimately land in circumstances where runaway accumulation occurs.

An additional gap in our story is that we have not probed irradiances below 675 W m^{-2} , whereas the outer edge of the conventional HZ for G stars is in the vicinity of 475 W m^{-2} , requiring nearly 10 bars of CO_2 for its maintenance. Aside from the irradiation being lower than we have probed, the CO_2 level is somewhat over twice the maximum value we considered. We cannot at present rule out the possibility that the climate/carbon equilibrium stabilizes as the outer HZ edge is approached. This in itself would be an interesting state of affairs, leading to the notion of “habitable bands” rather than a continuous HZ.

At lower irradiances than we have probed, which correspond to conditions nearer to the outer edge of the conventional HZ, CO_2 condensation will occur for high- CO_2 states, first in the upper atmosphere and then approaching the ground as irradiation decreases. This condensation has the dual effect on the planetary energy budget of keeping the upper atmosphere warmer than it would have been on the noncondensing adiabat, and through the radiative effects of CO_2 ice clouds. CO_2 ice clouds aloft have a cooling effect through increasing albedo, and a warming effect through their (infrared scattering) greenhouse effect. Regardless of whether the net effect is warming, cooling, or neutral, the cloud albedo further reduces the surface irradiation, making the energy limit more stringent than in clear-sky conditions and thus further reducing weathering as CO_2 increases. This would add to the destabilization of the climate-carbon equilibrium.

5.2. *Seafloor Weathering*

One important consideration is the potential contribution of low-temperature, off-axis hydrothermal basalt alteration, frequently referred to as “seafloor weathering,” which has been proposed as an alternative or complementary stabilizing,

temperature- and $p\text{CO}_2$ -sensitive CO_2 sequestration flux analogous to the continental weathering feedback (e.g., Francois & Walker 1992; Brady & Gislason 1997; Coogan & Gillis 2013; Coogan & Dosso 2015; Krissansen-Totton & Catling 2017; Krissansen-Totton et al. 2018; Coogan & Gillis 2018; Hayworth & Foley 2020). Some work has discounted its ability to act as a stabilizing feedback (Caldeira 1995; Abbot et al. 2012), but these conclusions have been questioned due to laboratory (Brady & Gislason 1997) and geochemical (Coogan & Gillis 2013; Coogan & Dosso 2015; Coogan & Gillis 2018) data that indicate an appreciable temperature dependence of seafloor weathering reactions, potentially allowing the process to accelerate under warmer climates and operate as a negative feedback, with important implications for the history of Earth (Krissansen-Totton & Catling 2017; Krissansen-Totton et al. 2018) and the habitability of exoplanets (Hayworth & Foley 2020; Chambers 2020). However, these modeling works generally ignore the throttling effect of clay formation, which plays such a fundamental role in the weakening of the continental silicate weathering feedback in the Maher & Chamberlain 2014 framework. If the waters flowing through seafloor basalts tend to reach their equilibrium concentration of weathering products before the formation of carbonates, then without a feedback between pore-water flow rates and global surface temperatures there is limited scope for seafloor weathering to operate as a thermostat. Developing a complete MAC-style model of seafloor weathering that accounts for the major controls on pore-water flow rates and the precipitation of relevant clay phases, as suggested in Graham & Pierrehumbert (2020), with first steps taken in Hakim et al. (2021), is a necessary next step toward evaluating the importance of seafloor weathering to the carbon cycle of Earth and other exoplanets. This is particularly crucial given the fact that clay formation on the seafloor was likely much more efficient in early Earth’s oceans (and in the oceans of abiotic exoplanets) due to the lack of biosilicifying organisms, which maintain the modern Earth’s ocean in a subsaturated state with respect to silica (Siever 1992; Kalderon-Asael et al. 2021). Silica is one of the weathering products that drives the formation of many of the clays that consume weathering-derived cations and reduce carbonate precipitation, decreasing the effectiveness of weathering at driving carbon sequestration; thus although seafloor clay precipitation (“reverse weathering”) has been suggested to exert its own form of negative feedback (e.g., Isson & Planavsky 2018; Krissansen-Totton & Catling 2020), it may also prevent traditional seafloor weathering from operating efficiently. The net impact on the carbon cycle of weathering-related processes occurring on the seafloor remains unclear (Krissansen-Totton & Catling 2020).

5.3. *Water Clouds*

In future work, it will be important to determine whether water clouds could stabilize the MAC weathering feedback. Water clouds affect the hydrology because their albedo further reduces the surface irradiation. This is true for both boundary layer clouds and clouds aloft, but clouds aloft in addition exert a warming influence through their greenhouse effect, which can partly compensate or even overwhelm the cooling effect of the albedo. We have cited some reasons to suspect that boundary layer water clouds may be absent in a high- $p\text{CO}_2$ regime, but if they are still present at, for example, the 1 bar climate but dissipate as $p\text{CO}_2$ increases further, then that would partly

offset the energy limit effects on precipitation due to the albedo of CO_2 . Insofar as **MAC** weathering is more sensitive to hydrology than to direct temperature effects, dissipation of high clouds could have the same effect on weathering, despite their warming influence. In cases where high clouds exert a dominant warming effect, though, the additional warming could enhance the desertification effect, which in our simulations contributes to the destabilizing weathering feedback. Generally speaking, it should be noted that the incremental albedo effect of clouds is muted in climates where albedo is already high due to CO_2 , and that the greenhouse effect of clouds can be muted if they lie below the radiating level of an optically thick CO_2 atmosphere.

5.4. Continental Configuration

The amount and spatial arrangement of land can have complex and difficult-to-predict impacts on continental weathering rates via changes to runoff and precipitation (Baum et al. 2022). It may be that certain continental configurations tend to produce positive-feedback behavior, while others produce negative-feedback behavior. Relatedly, topography heavily influences (and is influenced by) precipitation (Roe 2005) and erosion (Montgomery & Brandon 2002) rates, which in turn affect the thickness and age of soils (e.g., Heimsath et al. 2000; Owen et al. 2011), with direct impacts on silicate weathering rates (Ferrier & Kirchner 2008; Hilley et al. 2010; West 2012; Maher & Chamberlain 2014). Surface evolution driven by plate movements (e.g., Coy 2022) means that all of these factors may constantly coevolve on an Earth-like planet with plate tectonics. Further, planets in the “stagnant lid” mode (no plate tectonics; e.g., Foley 2019) may display systematic differences in topography (Guimond et al. 2022) and outgassing rates (Guimond et al. 2021), likely introducing further major variation into all of these factors controlling weathering rates and climate evolution. Correlations and feedbacks between the many variables controlling weathering fluxes could significantly change the picture we have presented, and a much broader parameter sweep and investigation of these issues is necessary.

5.5. Ocean Heat Transport

Modeling climate with a slab (as opposed to dynamical) ocean is a significant simplification, but we consider it unlikely to have a large impact on our qualitative results. Note first that our simulations are carried out without a seasonal cycle, so that the ocean response time is immaterial except insofar as it somewhat dampens surface-temperature response to synoptic variability. Additionally, study of Earth’s climate suggests that oceans carry a relatively small proportion of meridional heat transport, with the bulk carried by the atmosphere (Trenberth & Caron 2001). Moreover, there are robust reasons to expect the atmosphere to compensate for the absence of ocean heat transport (Farneti & Vallis 2013).

Nonetheless, ocean heat transport can increase atmospheric water vapor by spreading atmospheric convection out of a planet’s deep tropics, resulting in global-mean warming (Herweijer et al. 2005). Furthermore, in an icy climate, ocean heat transports can have considerable warming effects because a small amount of heat delivered to and under the sea-ice margin is very efficient at melting ice (e.g., Rose 2015). The latter is not a factor in the climates we explore, since they are

all too warm to support much ice, but it is well established that ocean heat transport and sea-ice dynamics have a strong influence on the CO_2 concentration at which a planet transitions into a snowball state (Pierrehumbert et al. 2011), generally requiring lower CO_2 for global glaciation than is the case for slab models. Inclusion of dynamical ocean and sea-ice effects would be crucial in order to definitively answer whether the low- CO_2 states the unstable system is attracted to on the cold side of the unstable equilibrium are snowballs. This is a question we do not attempt to resolve in the present simulations. We also note that some simulations of exoplanetary habitability in the middle and outer reaches of the HZ have found ocean heat transport to have a major effect on climate by warming the nightsides of synchronously rotating exoplanets, where they do not receive instellation from their parent stars (Yang et al. 2013, 2014, 2019a; Hu & Yang 2014). However, since our study is concerned with rapidly rotating exoplanets, this mechanism is less crucial.

5.6. Continental Lithology

We have considered only one mineral composition for the weatherable surface, but weathering behavior is sensitive to lithology (Hakim et al. 2021). Additionally, the continental crust would typically exhibit considerable spatial variations in lithology, driven by a multitude of tectonic processes. Such variations can accentuate the effect of continental configuration.

A possible exit route from uncontrolled CO_2 accumulation could arise through the power-law dependence of C_{eq} in Equation (4) (characterized by exponent n in Table 2), which allows for larger concentrations of weathering products in a given amount of water for planets with larger $p\text{CO}_2$, suggesting that further accumulation of CO_2 in the energetically limited regime could eventually reverse the sign of the weathering curve back into negative-feedback territory. This is the mechanism that allowed the subset of simulations that entered the parameterized energetically limited precipitation regime in the global-mean study of Graham & Pierrehumbert (2020) to avoid runaway CO_2 accumulation, instead equilibrating at hot temperatures with high $p\text{CO}_2$. In this scenario, the slope of the blue weathering curve in Figure 10 would eventually reverse and begin to increase again at high $p\text{CO}_2$, introducing a new, stable carbon cycle equilibrium at a $p\text{CO}_2 > P_2$. However, we note that the chemical equilibrium constants governing C_{eq} are negatively temperature dependent for many lithologies, such that the maximum concentration of weathering products decreases exponentially with increasing temperature, opposite to the behavior of kinetic rate constants and offsetting the power-law increase of C_{eq} with $p\text{CO}_2$ (Hakim et al. 2021). A set of weathering calculations including this effect led to even larger drops in global weathering rates with $p\text{CO}_2$ in the high- CO_2 simulations, exacerbating the bifurcation and hysteresis identified above. Still, there remains a possibility that weathering rates could, under some circumstances, begin to climb again at extremely high $p\text{CO}_2$ when CO_2 begins to cool the planetary surface instead of warm it. Further, some field measurements suggest that supercritical CO_2 forms carbonates extremely rapidly upon being brought into contact with basalts (McGrail et al. 2017), suggesting the intriguing possibility that weathering would increase greatly under supercritical conditions, providing another possible mechanism for the weathering curve to regain its negative feedback at extremely high $p\text{CO}_2$.

5.7. Spin State

This study focused on rapidly rotating planets orbiting Sun-like G stars. Carbon cycling on slowly rotating and tidally locked planets has received much less attention. Kite et al. (2011) found that WHAK-style silicate weathering can transform into a positive feedback for tidally locked planets with thin, CO₂-dominated atmospheres through a mechanism completely different from that explored here. Weathering-induced climate hysteresis on tidally locked planets with very limited water inventories has also been suggested (Ding & Wordsworth 2020). Other WHAK-based calculations have suggested a significant dependence of weathering rates on planetary rotation rate (Jansen et al. 2019) and enormous changes to weathering rates as a function of continental position on fully synchronous rotators (Edson et al. 2012). These effects are especially important since slowly rotating planets are expected to experience very efficient true polar wander, leading to continuous reorientation of their surfaces with respect to the substellar point on timescales comparable to that of the carbonate-silicate cycle as a result of mantle convection (Leconte 2018). Hydrological cycling on tidally locked planets displays subtle behavior with unclear implications for weathering rates (Labonté & Merlis 2020). MAC weathering calculations have not yet been applied to tidally locked climates, so it is unclear whether the mechanisms we have identified in this study will come into play in that context, but this is a crucial area for future research to evaluate the potential climate stability of planets orbiting M dwarfs, the most plentiful stars in the Universe (e.g., Catling & Kasting 2017).

6. Conclusion

In this study, we have calculated estimates of continental silicate weathering fluxes for Earth-like exoplanets by applying the MAC weathering model to output from GCM simulations of planetary climate under a variety of $p\text{CO}_2$ values and TOA instellations. Weathering rates and fluxes predicted according to MAC diverge profoundly from values calculated according to the more widely used WHAK model, particularly at lower instellations within the HZ. We have shown that for a considerable range of low instellations and high $p\text{CO}_2$ generally characteristic of the outer portions of the conventionally defined HZ, the common assumption that silicate weathering provides a stabilizing feedback on climate can break down, because the climate/carbon cycle equilibrium becomes unstable. The destabilization of the equilibrium arises because of the sensitivity of MAC weathering to hydrology, emphasizing a need for greater attention to the interplay of weathering and hydroclimate changes in the outer regions of the conventional HZ. Because of limitations in our modeling framework and parameter coverage, our results are not yet sufficient to conclude that the geochemically consistent HZ is contracted relative to the conventional HZ that only takes into account radiative and thermodynamic constraints, but it does reveal mechanisms whereby habitability can break down in the outer portions of the conventional HZ.

Acknowledgments



This work was previously published in somewhat modified form as a chapter of R.J.G.'s DPhil thesis (Graham 2022). We thank Itay Halevy and Vivien Parmentier for reviewing it as a thesis chapter. We also thank two anonymous reviewers that

provided useful feedback that significantly improved the manuscript. R.J.G. acknowledges support from the Clarendon Fund and Jesus College, Oxford. This work received support from the UK Science and Technologies Facilities Council Consolidated grant No. ST/W000903/1. This AETHER publication is also funded in part by the Alfred P. Sloan Foundation under grant No. G202114194.

Data Availability

Isca simulation outputs and Python scripts used to produce the figures in this paper are available for download at doi:[10.5281/zenodo.10995044](https://doi.org/10.5281/zenodo.10995044) (Graham & Pierrehumbert 2024).

ORCID iDs

R. J. Graham  <https://orcid.org/0000-0001-9289-4416>
R. T. Pierrehumbert  <https://orcid.org/0000-0002-5887-1197>

References

- Abbot, D. S. 2016, *ApJ*, **827**, 117
 Abbot, D. S., Cowan, N. B., & Ciesla, F. J. 2012, *ApJ*, **756**, 178
 Allan, R. P., Barlow, M., Byrne, M. P., et al. 2020, *NYASA*, **1472**, 49
 Bandstra, J. Z., & Brantley, S. L. 2008, in *Kinetics of Water–Rock Interaction*, ed. S. L. Brantley, J. D. Kubicki, & A. F. White (New York: Springer), 211
 Baranov, Y. I., Lafferty, W. J., & Fraser, G. T. 2004, *JMoSp*, **228**, 432
 Baum, M., Fu, M., & Bourguet, S. 2022, *GeoRL*, **49**, e98843
 Berner, R. 1994, *AmJS*, **294**, 56
 Betts, A. K., & Miller, M. J. 1993, in *The Representation of Cumulus Convection in Numerical Models*, ed. K. A. Emanuel & D. J. Raymond (Boston, MA: American Meteorological Society), 107
 Boer, G. J. 1993, *CIDy*, **8**, 225
 Brady, P., & Gislason, S. 1997, *GeCoA*, **61**, 965
 Brady, P. V. 1991, *JGR*, **96**, 18101
 Brantley, S. L., Kubicki, J. D., & White, A. F. 2008, *Kinetics of Water–Rock Interaction* (Berlin: Springer)
 Byrne, M. P., & O’Gorman, P. A. 2015, *JCLI*, **28**, 8078
 Caldeira, K. 1995, *AmJS*, **295**, 1077
 Carroll, S. A., & Knauss, K. G. 2005, *ChGeo*, **217**, 213
 Catling, D. C., & Kasting, J. F. 2017, *Atmospheric Evolution on Inhabited and Lifeless Worlds* (Cambridge: Cambridge Univ. Press)
 Chambers, J. 2020, *ApJ*, **896**, 96
 Chen, Y., & Brantley, S. L. 1998, *ChGeo*, **147**, 233
 Coogan, L., & Gillis, K. 2020, *E&PSL*, **536**, 116151
 Coogan, L. A., & Dosso, S. E. 2015, *E&PSL*, **415**, 38
 Coogan, L. A., & Gillis, K. 2018, *GeCoA*, **243**, 24
 Coogan, L. A., & Gillis, K. M. 2013, *GGG*, **14**, 1771
 Coy, B. P. 2022, Masters thesis, Univ. of Chicago
 Cronin, T. W. 2014, *JAtS*, **71**, 2994
 Ding, F., & Wordsworth, R. D. 2020, *ApJL*, **891**, L18
 Edson, A. R., Kasting, J. F., Pollard, D., Lee, S., & Bannon, P. R. 2012, *AsBio*, **12**, 562
 Edwards, J., & Slingo, A. 1996, *QJRMS*, **122**, 689
 Farneti, R., & Vallis, G. K. 2013, *JCLI*, **26**, 7151
 Feng, H., & Zhang, M. 2015, *NatSR*, **5**, 18018
 Ferrier, K. L., & Kirchner, J. W. 2008, *E&PSL*, **272**, 591
 Foley, B. J. 2019, *ApJ*, **875**, 72
 Foley, B. J., & Smye, A. J. 2018, *AsBio*, **18**, 873
 Francois, L. M., & Walker, J. 1992, *AmJS*, **292**, 81
 Frierson, D. M. W., Held, I. M., & Zurita-Gotor, P. 2006, *JAtS*, **63**, 2548
 Gaudi, B. S., Seager, S., Mennesson, B., et al. 2020, arXiv:2001.06683
 Ghiggi, G., Humphrey, V., Seneviratne, S. I., & Gudmundsson, L. 2019, *ESSD*, **11**, 1655
 Goldblatt, C., McDonald, V. L., & McCusker, K. E. 2021, *NatGe*, **14**, 143
 Golubev, S. V., Pokrovsky, O. S., & Schott, J. 2005, *ChGeo*, **217**, 227
 Gómez-Leal, I., Kaltenecker, L., Lucarini, V., & Lunkeit, F. 2018, *ApJ*, **869**, 129
 Goodwin, P. 2021, *Oxford Open Climate Change*, **1**, kgab007
 Gordon, I. E., Rothman, L. S., Hill, C., et al. 2017, *JQSRT*, **203**, 3
 Graham, R. 2022, PhD thesis, Univ. of Oxford
 Graham, R., Lichtenberg, T., & Pierrehumbert, R. T. 2022, *JGRE*, **127**, e2022JE007456

- Graham, R., & Pierrehumbert, R. 2020, *ApJ*, **896**, 115
- Graham, R., & Pierrehumbert, R. 2024, Data and code for “Carbon cycle instability for high-CO₂ exoplanets: implications for habitability” v1, Zenodo, doi:10.5281/zenodo.10995044
- Graham, R. J. 2021, *AsBio*, **21**, 1406
- Guimond, C. M., & Cowan, N. B. 2018, *AJ*, **155**, 230
- Guimond, C. M., Noack, L., Ortenzi, G., & Sohl, F. 2021, *PEPI*, **320**, 106788
- Guimond, C. M., Rudge, J. F., & Shorttle, O. 2022, *PSJ*, **3**, 66
- Gutowski, W. J., Jr, Gutzler, D. S., & Wang, W.-C. 1991, *JCLI*, **4**, 121
- Guzewich, S. D., Way, M. J., Aleinov, I., et al. 2021, *JGRE*, **126**, e06825
- Hakim, K., Bower, D. J., Tian, M., et al. 2021, *PSJ*, **2**, 49
- Halevy, I., Pierrehumbert, R. T., & Schrag, D. P. 2009, *JGRD*, **114**, D18112
- Haqq-Misra, J., Kopparapu, R. K., Batalha, N. E., Harman, C. E., & Kasting, J. F. 2016, *ApJ*, **827**, 120
- Hayworth, B. P., & Foley, B. J. 2020, *ApJ*, **902**, L10
- Heimsath, A. M., Chappell, J., Dietrich, W. E., Nishiizumi, K., & Finkel, R. C. 2000, *Geo*, **28**, 787
- Held, I. M., & Soden, B. J. 2006, *JCLI*, **19**, 5686
- Herweijer, C., Seager, R., Winton, M., & Clement, A. 2005, *TellA*, **57**, 662
- Hilley, G., Chamberlain, C., Moon, S., Porder, S., & Willett, S. 2010, *E&PSL*, **293**, 191
- Hu, Y., & Yang, J. 2014, *PNAS*, **111**, 629
- Isson, T. T., & Planavsky, N. J. 2018, *Natur*, **560**, 471
- Jansen, T., Scharf, C., Way, M., & Del Genio, A. 2019, *ApJ*, **875**, 79
- Kadoya, S., Krissansen-Totton, J., & Catling, D. C. 2020, *GGG*, **21**, e2019GC008734
- Kadoya, S., & Tajika, E. 2019, *ApJ*, **875**, 7
- Kalderon-Asael, B., Katchinoff, J. A., Planavsky, N. J., et al. 2021, *Natur*, **595**, 394
- Kasting, J. F., & Ackerman, T. P. 1986, *Sci*, **234**, 1383
- Kasting, J. F., & Harman, C. E. 2013, *Natur*, **504**, 221
- Kasting, J. F., Whitmire, D. P., & Reynolds, R. T. 1993, *Icar*, **101**, 108
- Kite, E., Gaidos, E., & Manga, M. 2011, *ApJ*, **743**, 41
- Kitzmann, D. 2017, *A&A*, **600**, A111
- Knauss, K. G., Nguyen, S. N., & Weed, H. C. 1993, *GeCoA*, **57**, 285
- Knutti, R., Rugenstein, M. A., & Hegerl, G. C. 2017, *NatGe*, **10**, 727
- Kopparapu, R. K. 2013, *ApJ*, **767**, L8
- Kopparapu, R. K., Ramirez, R., Kasting, J. F., et al. 2013, *ApJ*, **765**, 131
- Krissansen-Totton, J., Arney, G. N., & Catling, D. C. 2018, *PNAS*, **115**, 4105
- Krissansen-Totton, J., & Catling, D. C. 2017, *NatCo*, **8**, 15423
- Krissansen-Totton, J., & Catling, D. C. 2020, *E&PSL*, **537**, 116181
- Kump, L. R. 2018, *RSPTA*, **376**, 20170078
- Kundzewicz, Z. W. 2008, *Ecohydrol. Hydrobiol.*, **8**, 195
- Labonté, M.-P., & Merlis, T. M. 2020, *ApJ*, **896**, 31
- Le Hir, G., Donnadiou, Y., Godderis, Y., et al. 2009, *E&PSL*, **277**, 453
- Leconte, J. 2018, *NatGe*, **11**, 168
- Li, J., Scinocca, J., Lazare, M., et al. 2006, *JCLI*, **19**, 6314
- Maher, K., & Chamberlain, C. 2014, *Sci*, **343**, 1502
- Manabe, S. 1969, *MWRv*, **97**, 739
- McGrail, B. P., Schaef, H. T., Spane, F. A., et al. 2017, *Environ. Sci. Technol. Lett.*, **4**, 6
- Menou, K. 2015, *E&PSL*, **429**, 20
- Mlawer, E. J., Payne, V. H., Moncet, J. L., et al. 2012, *RSPTA*, **370**, 2520
- Montgomery, D. R., & Brandon, M. T. 2002, *E&PSL*, **201**, 481
- Myhre, G., Forster, P., Samset, B., et al. 2017, *BAMS*, **98**, 1185
- Myhre, G., Samset, B. H., Hodnebrog, Ø., et al. 2018, *NatCo*, **9**, 1922
- Noack, L., Rivoldini, A., & Van Hoolst, T. 2017, *PEPI*, **269**, 40
- Oelkers, E. H., & Schott, J. 2001, *GeCoA*, **65**, 1219
- Owen, J. J., Amundson, R., Dietrich, W. E., et al. 2011, *ESPL*, **36**, 117
- Oxburgh, R., Drever, J. I., & Sun, Y.-T. 1994, *GeCoA*, **58**, 661
- O’Gorman, P. A., Allan, R. P., Byrne, M. P., & Previdi, M. 2012, *SGeo*, **33**, 585
- O’Gorman, P. A., & Schneider, T. 2008, *JCLI*, **21**, 3815
- Palandri, J. L., & Kharaka, Y. K. 2004, A compilation of rate parameters of water-mineral interaction kinetics for application to geochemical modeling 2004-1068, Geological Survey (Menlo Park, CA)
- Paradise, A., & Menou, K. 2017, *ApJ*, **848**, 33
- Paradise, A., Menou, K., Valencia, D., & Lee, C. 2019, *JGRE*, **124**, 2087
- Penman, D. E., Rugenstein, J. K. C., Ibarra, D. E., & Winnick, M. J. 2020, *ESRv*, **209**, 103298
- Penn, J., & Vallis, G. K. 2018, *ApJ*, **868**, 147
- Perrin, M., & Hartmann, J. 1989, *JQSRT*, **42**, 311
- Pierrehumbert, R. T. 1999, *GMS*, **112**, 339
- Pierrehumbert, R. T. 2002, *Natur*, **419**, 191
- Pierrehumbert, R. T. 2010, Principles of Planetary Climate (Cambridge: Cambridge Univ. Press)
- Pierrehumbert, R. T., Abbot, D. S., Voigt, A., & Koll, D. 2011, *AREPS*, **39**, 417
- Quanz, S. P., Ottiger, M., Fontanet, E., et al. 2022, *A&A*, **664**, A21
- Ramirez, R. M., Kopparapu, R. K., Lindner, V., & Kasting, J. F. 2014, *AsBio*, **14**, 714
- Rimstidt, J. D., Brantley, S. L., & Olsen, A. A. 2012, *GeCoA*, **99**, 159
- Roe, G. H. 2005, *AREPS*, **33**, 645
- Romps, D. M. 2020, *JCLI*, **33**, 3413
- Rose, B. E. 2015, *JGRD*, **120**, 1404
- Russell, G. L., Lacy, A. A., Rind, D. H., Colose, C., & Opstbaum, R. F. 2013, *GeoRL*, **40**, 5787
- Schneider, T., Kaul, C. M., & Pressel, K. G. 2019, *NatGe*, **12**, 163
- Schott, J., & Berner, R. A. 1985, in The Chemistry of Weathering, ed. J. I. Drever (Dordrecht: Springer), 35
- Sellers, W. D. 1969, *JApMe*, **8**, 392
- Shibuya, T., & Takai, K. 2022, *PEPS*, **9**, 1
- Siever, R. 1992, *GeCoA*, **56**, 3265
- Siler, N., Roe, G. H., Armour, K. C., & Feldl, N. 2019, *CIDy*, **52**, 3983
- Solomatova, N. V., & Caracas, R. 2021, *SciA*, **7**, eabj0406
- Stephens, G. L., O’Brien, D., Webster, P. J., et al. 2015, *RvGeo*, **53**, 141
- Strogatz, S. 1994, *ComPh*, **8**, 45
- The LUVOIR Team 2019, arXiv:1912.06219
- Thomson, S. I., & Vallis, G. K. 2019a, *QJRMMS*, **145**, 2627
- Thomson, S. I., & Vallis, G. K. 2019b, *Atmos*, **10**, 803
- Trenberth, K. E., & Caron, J. M. 2001, *JCLI*, **14**, 3433
- Turbet, M., Forget, F., Leconte, J., Charnay, B., & Tobie, G. 2017, *E&PSL*, **11**, 11
- Vallis, G. K., Colyer, G., Geen, R., et al. 2018, *GMD*, **11**, 843
- Vecchi, G. A., Soden, B. J., Wittenberg, A. T., et al. 2006, *Natur*, **441**, 73
- Von Paris, P., Selsis, F., Kitzmann, D., & Rauer, H. 2013, *AsBio*, **13**, 899
- Walker, J. C. G., Hays, P. B., & Kasting, J. F. 1981, *JGR*, **86**, 9776
- Walters, D., Baran, A. J., Boutle, I., et al. 2019, *GMD*, **12**, 1909
- Way, M. J., Aleinov, I., Amundsen, D. S., et al. 2017, *ApJS*, **231**, 12
- Weissbart, E. J., & Rimstidt, J. D. 2000, *GeCoA*, **64**, 4007
- Welch, S., & Ullman, W. 1996, *GeCoA*, **60**, 2939
- West, A. J. 2012, *Geo*, **40**, 811
- Winnick, M. J., & Maher, K. 2018, *E&PSL*, **485**, 111
- Wolf, E., Haqq-Misra, J., & Toon, O. 2018, *JGRD*, **123**, 11861
- Wordsworth, R., Forget, F., & Eymet, V. 2010, *Icar*, **210**, 992
- Wordsworth, R. D., & Pierrehumbert, R. T. 2013, *ApJ*, **778**, 154
- Xiong, J., Yang, J., & Liu, J. 2022, *GeoRL*, **49**, e99599
- Yang, J., Abbot, D. S., Koll, D. D., Hu, Y., & Showman, A. P. 2019a, *ApJ*, **871**, 29
- Yang, J., Boué, G., Fabrycky, D. C., & Abbot, D. S. 2014, *ApJL*, **787**, L2
- Yang, J., Cowan, N. B., & Abbot, D. S. 2013, *ApJL*, **771**, L45
- Yang, J., Leconte, J., Wolf, E. T., et al. 2019b, *ApJ*, **875**, 46